DEVELOPMENT AND CHARACTERIZATION OF A VIRTUAL IMPACTOR TYPE DUST FLOW CONCENTRATOR

DEVELOPMENT AND CHARACTERIZATION OF A VIRTUAL IMPACTOR TYPE DUST FLOW CONCENTRATOR

By

HONGBING WANG, B.ENG, M.ENG.

A Thesis

Submitted to the School of Graduate Studies

in Partial Fulfillment of the Requirements

for the Degree

Master of Applied Science

McMaster University

MASTER OF APPLIED SCIENCE (2005) McMaster University

(Mechanical Engineering) Hamilton, Ontario

TITLE: Development and Characterization of a Virtual Impactor Type Dust Flow Concentrator

AUTHOR: Hongbing Wang

B.Eng. (Xi'an Jiaotong University, P. R. China)

M.Eng. (Xi'an Jiaotong University, P. R. China)

SUPERVISORS: Dr. Chan Y. Ching and Dr. Dan Ewing

Department of Mechanical Engineering

NUMBER OF PAGES: xiv, 94

ABSTRACT

A virtual impactor type dust flow concentrator was developed and an experimental investigation was performed to characterize the hydraulic and particulate matter (PM) separation performance of the device. In particular, the pressure drop characteristics, the ratio of the flow through the two branches, and the PM concentration in the minor and main branch of the flow concentrator were evaluated using experiments on a diesel exhaust rig and an air rig. Tests were performed to examine the effect of the inlet flow Reynolds number, the inlet tube lip position relative to the concentration probe, and the flow distribution between the minor and main branches. Numerical simulations were also performed for a simplified concentrator geometry to examine the flow streamlines and pressure drop. The results showed that the ratio of the concentration in the minor and main flow branches changed as the flow rate in these branches changed, reaching a maximum at a minor flow ratio that depended on the lip position. It was observed the difference of the particulate matter concentration in the minor and main branch was greater for higher inlet Reynolds number. For example, the concentration ratio increased 50% as the Reynolds number increased from 2,200 to 25,700. A similar result was observed when the inlet tube lip was moved further into the concentration body. The pressure losses seem to be mainly caused by the changes in flow directions and the change in the cross sectional areas.

ACKNOWLEDGEMENTS

I would like to express gratitude to my supervisors, Dr. C. Y. Ching and Dr. D. Ewing for their invaluable guidance and support. I would like to express my appreciation to Dr. J.S. Chang for his assistance for this work. I would also like to thank a great number of persons for their timely help to complete this work.

Technicians, Mr. Andrew Buyers, Mr. Ron Lodewyks, Mr. Joe Verhaege, Mr. Greg Ksiazek, and Mr. Dave Shick gave great technical help in constructing the test rig and solving many experimental problems.

Fraser Charles and John Colenbrander, colleagues in the diesel engine pollution control group, helped a great deal during the engine tests. The members in the natural gas pollution control group also gave me much assistance and suggestions while working together for nearly two years.

Special thanks to my TMRL Deep-Homers teammates and all of my friends in the Thermal Management Research Laboratory for their help and support.

I also want to express my appreciation to my mother and my sisters for their encouragement and support. I would like to dedicate this work to my wife and my two lovely sons.

TABLE OF CONTENTS

LIST OF FIGURES

LIST OF TABLES

NOMENCLATURE

a	Fluid thermal diffusivity coefficient	m^2/s
C	Cunningham correction factor	
C_p	The ratio of the pressure drop to the inlet dynamic pressure	
d_p	Particle diameter	m
D	Inside diameter of the inlet tube	m
D_p	Particle diffusion coefficient	m^2/s
g	Gravitational acceleration rate	m/s^2
$\dot{M}$	Mass flow rate of diesel engine exhaust	kg/hr
$\dot{M}_1$, $\dot{M}_{total}$	Mass flow rate of the inlet flow	kg/hr
$\dot{M}_2$, $\dot{M}_{main}$	Mass flow rate of the main branch flow	kg/hr
$\dot{M}_3$, $\dot{M}_{minor}$	Mass flow rate of the minor branch flow	kg/hr
N	Particulate matter mass concentration	mg/m^3
N_1, N_{inlet}	PM mass concentration in the inlet flow	mg/m^3
N_2, N_{main}	PM mass concentration in the main branch flow	mg/m^3
N_3, N_{minor}	PM mass concentration in the minor branch flow	mg/m^3
N_{inlet}	PM mass concentration at the inlet	mg/m^3
N_w	PM mass concentration at the wall	mg/m^3

P	Static pressure	Pa
$P_{main,\ inlet}$	Pressure at the central inlet of the main branch	Pa
P_{inlet}	Pressure at the center of the flow inlet	Pa
Q	Volume flow rate of the air	m^3/s
Q_1, Q_{total}	Volume flow rate of the inlet air flow	m^3/s
Q_2, Q_{main}	Volume flow rate of the main branch air flow	m^3/s
Q_3, Q_{minor}	Volume flow rate of the minor branch air flow	m^3/s
Re	Reynolds number	
R_N	Ratio of mass concentration of particulate matter in the minor flow to the main flow	
S	Inlet tube lip position relative to the concentration probe	m
S_c	Schmidt number	
S_t	Particle stokes number	
T	Fluid temperature	°C
$\overline{U}$	Fluid velocity (vector)	m/s
V_{in}	The mean velocity of the inlet flow	m/s
V_{max}	The maximum velocity at the inlet flow	m/s
W_0	Inside diameter of the inlet tube	m
W_1	Inside diameter of the minor outlet	m
X_{total}	Total length of the line in x direction	m
Y_{total}	Total length of the line in y direction	m

Greek

ν	Fluid kinematic viscosity	m^2/s
μ	Fluid dynamic viscosity	kg/(m•s)
ρ	Fluid density	kg/m^3
ρ_p	Particle material density	kg/m^3
τ_p	Particle response time	s
τ_c	Time interval between particle collision	s
θ	Angle between the liquid column and the horizontal plane	degree
ΔL	Liquid column length in manometer	m
ΔP	Pressure drop from the inlet to the outlet in simulation	Pa
ΔP_1	Pressure drop from the inlet to the outlet in air tests	Pa
ΔP_2	Pressure drop from the chamber to the outlet in air tests	Pa
ΔP_3	Pressure drop from the minor branch to the outlet in air tests	Pa
ΔP_4	Pressure drop from the main branch to the outlet in air tests	Pa
ΔP_5	Pressure drop from inlet to the main flow outlet in engine rig	Pa
ΔP_{V1}	Pressure drop across the inlet flow Venturi	Pa
ΔP_{V2}	Pressure drop across the main branch flow Venturi	Pa

Chapter 1 Introduction

There is increasing concern about the effect of the respirable particulate matter on human health due to the increasing presence of these fine particles in the atmosphere. Respirable particulate matter is typically defined as particulate matter with a diameter less than 3.5μm (Szymanski and Liu, 1989). It is increasingly recognized that the finer particulates are capable of penetrating deeper into the respiratory system and hence cause pathological changes. Their chemical components also play an important role depending on the ingredients. They are associated with sulfate, nitrate, trace metals, ammonium ions and carbon-containing compounds. These particles are generally defined in four categories (Kittelson, 1998) according to particle diameter: coarse particles (> 2.5 μm), fine particles (≤ 2.5 μm), ultrafine particles (< 0.1 μm), and nanoparticles (< 0.05 μm).

These respirable particles are frequently produced in mechanical processes and mainly in gas-particle conversion processes, such as coal and oil combustion, wood burning, waste incineration, and metal mining. Diesel engines are widely used in heavy-duty trucks and buses in North America and diesel engines are considered one of the most realistic short-term solutions to decrease CO_2 emissions. Diesel engines traditionally have high particulate matter emission and much of these are fine or ultrafine particles. The bulk of the particle number produced by diesel engines are nucleation mode particles (< 50 nm) or accumulation mode particles (50-150 nm). Normally, the former is made up of aerosols and the latter is carbon soot (Johnson, 2003). There is stringent regulations for

diesel engines. For example, the standards from the United States Environmental Protection Agency (Raber, 1997) maintain the allowed levels of 50 $\mu g\ m^{-3}$ annual average concentration of PM10 (particles smaller than 10 μm in diameter) and add an annual average standard of 15 $\mu g\ m^{-3}$ for fine particles PM2.5 (particles smaller than 2.5 μm in diameter).

The particulate matter emissions can be removed by improving the internal process, such as employing a more efficient combustion technology or a cleaner burning fuel (Liu, et al, 2003), or by adding emission control devices, such as diesel particulate filters. These devices have large particulate collection efficiencies but they impose a back pressure on the engine that increases as soot is loaded and they must be periodically regenerated. This results in higher energy consumption and requirement on high material strength. Thus, there would be interests in developing technologies with low pressure drop. Electrostatic precipitators are one technology that can be used to remove particulate matter with low pressure drop. However, the size of this device would have to be large to treat the particulate matter of the full exhaust flow effectively. Thus, one strategy is to develop a system to concentrate the particulate matter in a low flow stream before the electrostatic precipitator is applied. This was adopted as part of an integrated pollution control system being developed for small scale combustion based power generators to remove fine particles from the emissions effectively and economically before treating the gaseous pollutant.

A virtual impactor was investigated as the dust flow concentrator in this study. In a virtual impactor, the dust flow is divided into two flow streams. The diluted dust flow

has a higher flow rate and a lower particulate matter concentration while the concentrated dust flow has a lower flow rate and a higher particulate matter concentration. The concentrated dust flow would then pass through the electrostatic precipitator and the particulate matter would be removed.

The objective of this work was to develop a virtual impactor type dust flow concentrator with a cutpoint size on the order of 0.1 μm to 0.3 μm. The development of this concentrator was initiated using a numerical simulation of the flow field to examine the flow streamline distribution and pressure drop coefficient. A dust flow concentrator prototype was then fabricated and tested. The pressure drop characteristics were tested in an air and diesel engine exhaust test facilities. The separation of the particulate matter was examined for the diesel engine exhaust emissions.

The work here is presented in six chapters. In chapter two, the properties of diesel engine exhaust, application of diesel particulate filters, dust removal equipment, and virtual impactors are reviewed. The experimental facilities and methodology are presented in chapter three, while the results are presented in chapter four. Finally, in chapters five and six, the concluding remarks and recommendations are provided. The numerical simulation of the flow is also presented in the appendix.

Chapter 2 Literature Review

This chapter provides a review of the particulate matter characteristics of the in diesel engine emissions and the characteristics of gas-particle two-phase flows. The pollutant control technologies in diesel engines and gas solid separators are then reviewed. Finally, the approaches used to characterize virtual impactors are reviewed.

2.1 Particulate Matter in Diesel Engine Emissions

The emissions from diesel engines depend on the fuel and operating conditions for the diesel engine. Diesel engines typically produce 10 to100 times more particulate matter than gasoline engines (Kittleson, 1998). The particulate matter in diesel exhaust has been defined as the matter present after the exhaust has been diluted and cooled, typical of the process that occurs when diesel exhaust is emitted to the ambient. The particulate matter can be measured by sampling filters or by the method based on the opacity of the exhaust (SAE, 1996).

The particulate matter in this diluted diesel exhaust consist mainly of highly agglomerated solid carbonaceous material and ash, and volatile organic and sulfur compounds (Kittelson, 1998). A typical composition of the particulate matter for the U.S. Heavy Duty Transient Test is shown in Figure 2.1. In this case, the largest component is carbon, in a form of solid agglomerates. The solid agglomerates are the residue of the solid carbon that has not been oxidized. The solid carbon is formed during combustion in

the locally rich regions. A fraction of the fuel is not fully oxidized and results in volatile or soluble organic compounds, termed the soluble organic fraction, in the exhaust. Most of the sulfur in the fuel is oxidized to SO_2, but a fraction is oxidized to SO_3 leading to the formation of sulfuric acid and sulfates in the exhaust. Metal compounds in the fuel and lubrication oils also lead to a small amount of inorganic ash (Kittelson, 1998). The fraction associated with unburned fuel and lube oil varies with engine design and operating condition. Johnson (2003) reported soluble organic fraction values are highest at light engine loads when exhaust temperatures are low.

Kittelson (1998) observed that the particle size and weight distribution had a tri-modal distribution shown in Figure 2.2. The largest number of particles occurred in the nuclei-mode with size between 5 nm and 50 nm. The nuclei mode primarily consists of volatile organic and sulfur compounds formed during exhaust dilution and cooling, but also contains some solid carbon and metal compounds. This mode typically contained more than 90% of the particle number but only 1 to 20% of the particle mass. Most of the mass occurred in the accumulation-mode with particle size between 50 nm and 1 μm. The peak in the distribution and the particle mass occurred in particles with diameters between 0.1 and 0.3 μm. These tend to be carbonaceous agglomerates with associated absorbed materials. The coarse mode with particle size larger than 1 μm has 5 to 20% of the particle mass. The coarse mode particles are generated by re-entrainment of particles deposited on engine and exhaust system surfaces.

The particles present in the atmosphere are characterized in four categories: PM10 ($d_p < 10$ μm), fine particles ($d_p < 2.5$ μm), ultrafine particles ($d_p < 0.1$ μm), and

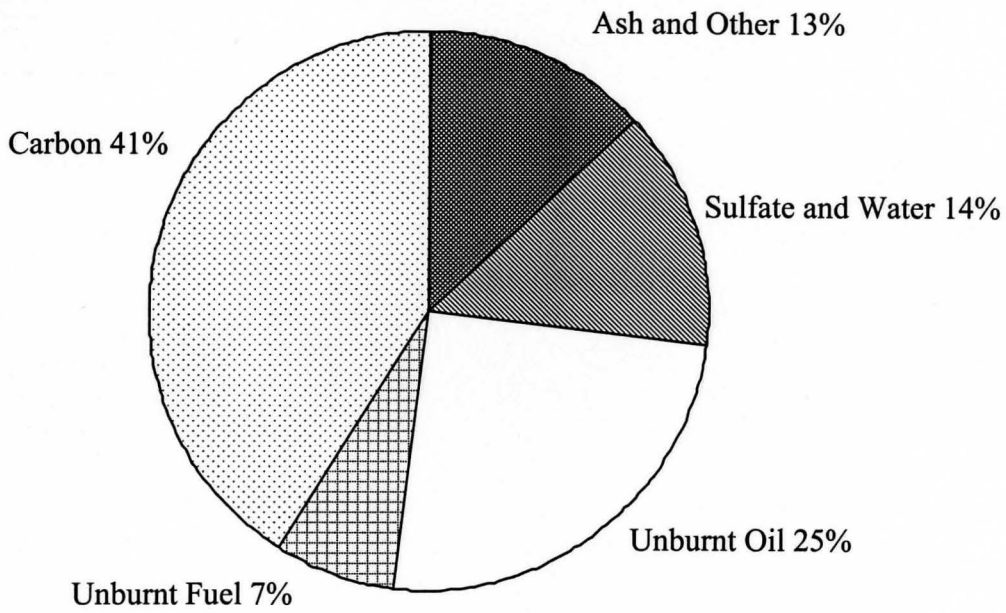

Figure 2.1 Typical diesel exhaust composition (Kittelson, 1998)

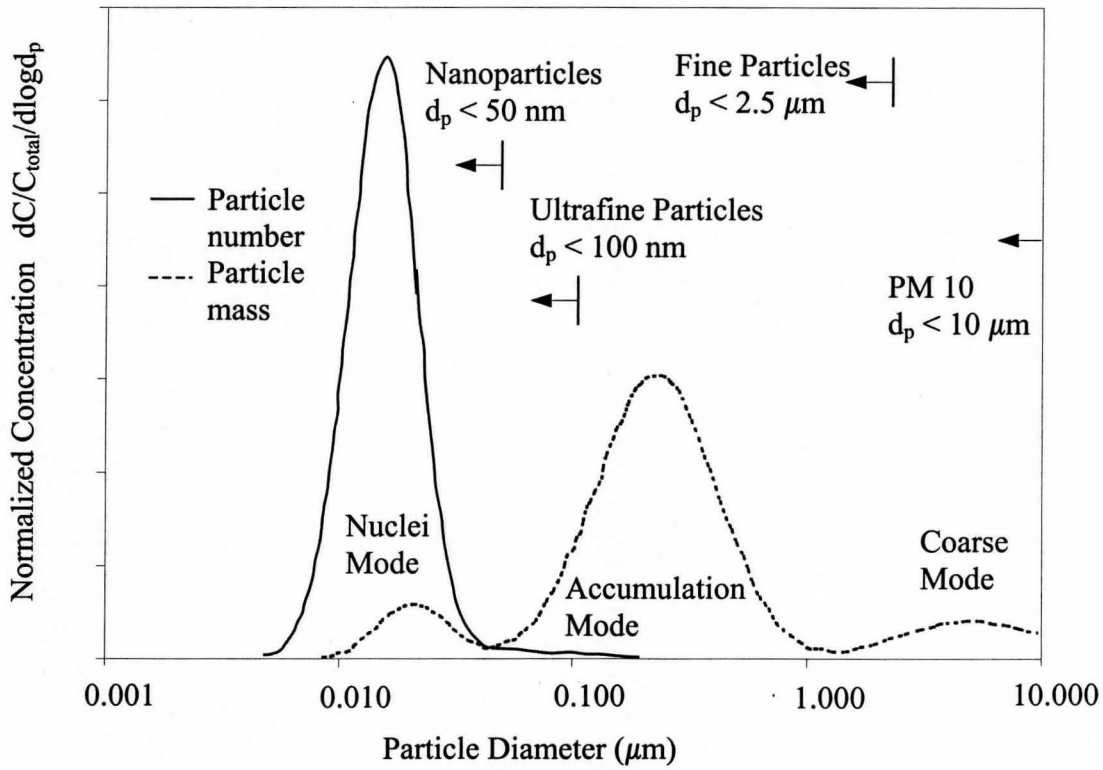

Figure 2.2 Typical exhaust particle size distribution (Kittelson, 1998)

nanoparticles ($d_p < 0.05$ μm). For diesel engines, highest percentage in term of the mass concentration emitted by engines is fine particles, while highest percentage in term of number concentration is nanoparticles. The composition of particles present in the diesel exhaust depends on where and how the particles are sampled from the exhaust. In particular, when the diesel exhaust gas is diluted and cooled, the mechanisms of nucleation, condensation, and adsorption change the volatile organic to solid and liquid particulate matter (Kittelson, 1998). Thus, the details of the dilution and cooling processes determine the relative amounts of material that adsorb or condense onto existing particles and nucleate to form new particles. The particulate matter concentration varies with the engine type and operating conditions. Particularly, the PM concentration increases with an increase in the fuel-air ratio in the engine. At normal fuel-air ratios, the PM volume concentrations for representative direct injection engines and indirect injection engines range from 10^3 to 10^6 $\mu m^3/cm^3$ (Kittleson, 1998).

The particle size has a significant impact on its effect in the atmosphere. Particles with diameter in the range from 0.1 to 10 μm reside in the atmosphere for approximately one week. The finer particles are likely to coagulate with accumulation mode particles and last the same time as larger particles (Harrison, 1996). The specific surface area of diesel exhaust particles is typically 100 m^2/g (Jakab et al., 1992). This large surface area is available for adsorption and chemical reactions with other constituents in the atmosphere. The adverse effect of particulate matter on human health are more linked with particles in the ultrafine and nanoparticle diameter range. Dockery et al (1993) reported that the number of particles and particle surface area per unit mass increases with

decreasing particle size. Warheit (1990) reported that the particles tend to be non-toxic in μm size range but those in the nm range are more toxic. It was reported that the efficiency of deposition in the human respiratory tract depends on particle size and, in particular, the deposition in lungs increases with decreasing particle size (Kittelson, 1998). There is increased interest in reducing the particulate matter from diesel engines. It is important to evaluate the effect of the changes of technologies on particulate number. Bagley et al (1996) found that the particulate matter mass concentration was reduced while the number concentration increased sharply in the tests on a direct injection diesel engine that had a high pressure (150 MPa peak injection pressure) precisely controlled fuel injection system. This indicates there was an increase in finer particles, which could have a greater impact on human health.

Thus, it is necessary to develop post-combustion technologies that can remove the fine particles from the diesel exhaust. The particulate matter control technology and the characteristics of gas-particle two-phase flows are discussed below.

2.2 Gas-Particle Two-Phase Flows

The development of gas-solid phases depends on the constituents involved and the relative velocity and concentration of these phases. A comparison of particle size in various multiphase systems is shown in Figure 2.3. These systems differ greatly in the solid components and particle sizes. Gas-particle flow can be classified as dilute or dense flow according to the flow characteristics (Crowe, 1982). In dilute flow, the particle motion is controlled by the surface and body forces on the particle, while in dense flow, it

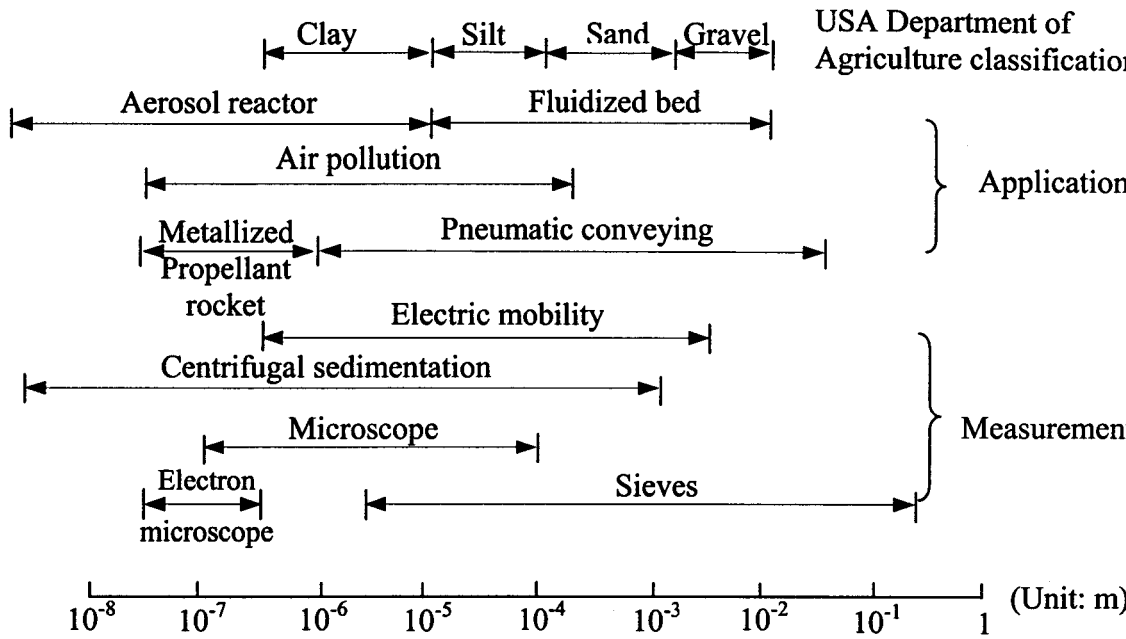

Figure 2.3 Magnitudes of particle size in gas-solid system (Soo, 1967)

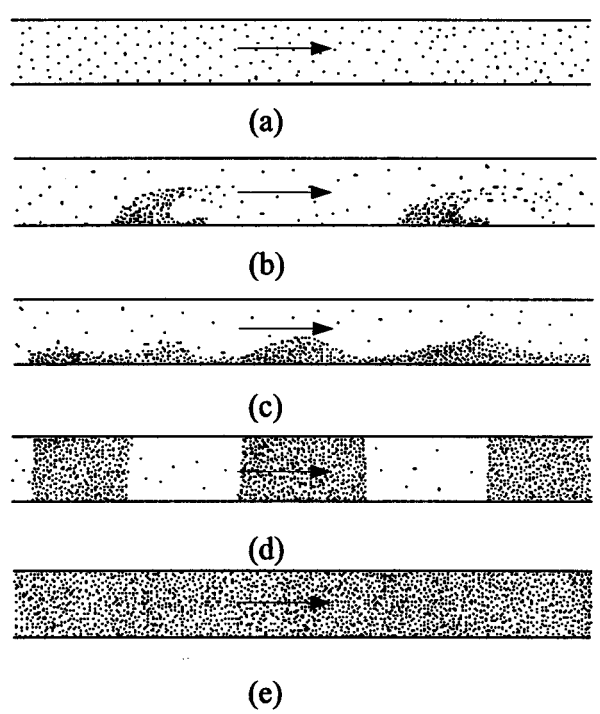

Figure 2.4 Horizontal flow patterns of gas-particle mixture: (a) dilute suspension flow, (b) sedimentation of particles and dune formation, (c) stratified flow, (d) plug flow, (e) moving bed flow (Fan and Zhu, 1998)

is controlled by particle-particle collisions or interactions. The typical flow patterns that may arise in a horizontal flow of a gas with solid particles are shown in Figure 2.4. These patterns happen for a given gas flow rate at the inlet and different particle loadings. At a very low solids concentration, particles are fully suspended and quite uniformly dispersed throughout the pipe, as shown in Figure 2.4(a). When the particle loading increases, particles tend to settle at the bottom of the pipe and may slide over other particles, as shown in Figure 2.4(b). Particle dunes are formed and particle flow moves from one dune to another and undergoes alternating acceleration and deceleration. A further increase in the particle loading yields a stratified flow with a wavy interface, as shown in Figure 2.4(c), and finally the particles form solid plugs characterized by the intermittent flow of gas and solids in alternating plugs as shown in Figure 2.4(d). With the increase in particle loading, a large portion of solids stay stationary at the bottom and the solids travel in the form of ripples at the top portion of the pipe. When the gas is accelerated to a relatively high velocity, the bed formed by the deposited particles begins to move with the gas phase, thus a moving bed flow occurs, as shown in Figure 2.4(e).

The characteristics of dilute and dense flows are compared in Table 2.1. The two kinds of flow primarily differ in the particle concentrations. Several criteria were proposed to differentiate the flow regimes. Crowe (1982) proposed that this could be done using the ratio of the particle response time (τ_p) to the time between collision (τ_c). When $\tau_p < \tau_c$, a particle has time to respond to the local gas velocity field before the next collision, so its motion is dominated by the aerodynamic forces and the flow is a dilute flow. When $\tau_p > \tau_c$, the flow is a dense flow. The ratio of τ_p/τ_c depends on loading, gas

Table 2.1 Comparison of dilute and dense suspension (Soo, 1989)

Property	**Dilute suspension**	**Dense suspension**
Relative motion between particles	Large	Small
Particle-particle interactions	Weak	Strong
Particle diffusivity	Large	Small
Apparent particle viscosity	Due to gas-particle interaction	Due to particle-particle interaction and gas –particle interaction
Flow regime in application	Steady, turbulent	Pseudolaminar to unsteady and stratified
Motion above minimum transport velocity	Stable	Unstable
Analogy in molecular system	Rarefied gas flow	Molecular theory of liquids or kinetic theory of gas

velocity gradient, and the spread of the particle size distribution (Crowe, 1981). Elghobashi (1994) proposed the flow is dilute when the particulate phase volume fraction is less than 10^{-3}. Fan and Zhu (1998) proposed the criteria of the mass flow ratio of solids to gas, the volumetric concentration of particles, the extent of particle-particle interaction, the mixture pressure drop against gas velocity.

Another characteristic in these flow is the forces exerted on the particles. The forces may be classified into three groups: forces through the interface between gas and particles, forces due to interactions between particles, and forces imposed by external fields, as summarized in Table 2.2. The first two groups are internal forces while the latter are external forces that depend on the fields of acceleration imposed on the gaseous suspension. The internal forces are due to the interactions between particles and between gas and particles in the flow field.

The approaches to modeling gas-particle flows vary with the characteristics of the flow. In dense gas-particle flow where interparticle collisions are dominant, the kinetic theory can be applied by assuming the collisions are the only mechanism for the transport of mass, momentum and energy of the particles. In this approach, the dynamic properties of the solid phase are postulated to be analogous to those of gas molecules (Culick, 1964). The application of this approach on fluidization and pneumatic transport systems was reported by Gidaspow (1993). For gas flow through a packed bed or an unsuspended portion of a particle transport system, Ergun (1952) proposed a semiempirical equation for the pressure drop with flow conditions. This equation also describes the limiting situation of a dense suspension system. The dispersed particle phase flows can be

Table 2.2 Summary of forces on particles in gas-particle flow

Classification	**Name or effect**	**Mechanisms**
Internal forces- due to interaction with gas phase	Drag force	Slip velocity between two phases
	Basset force	Relative acceleration between two phases
	Saffman force	Velocity gradient in gas fields
	Magnus force	Particles' rotation
	Diffusiophoresis	Concentration gradient; valid for fields containing vapor
	Thermophoresis	Field temperature gradient, also called radiometric forces
	Piezophoresis	Pressure gradient; dominant in filter flow
	Photophoresis	Temperature gradient in non-uniform radiation, also called radiometric forces
Internal force- due to interaction with particles	Collision force	Collisions between particle-wall and particle-particle
	Electrostatic force	Between charged particles; quantified by Coulomb's law
	Van der Waals force	Molecular or atomic interactions due to interacting dipoles
External forces	Gravitational force	The Earth
	Electric force	External electric fields
	Magnetic force	External magnetic fields

modeled by either one-way or two-way coupling. In a model based on one-way coupling, it is assumed that the particulate matter has a negligible effect on the gas properties so the motions of particles are controlled by the gas flow field. In a two-way coupling model, the effects of particles on the gas phase are included. In such a model, the existence of particles affect the local flow field and transport properties of the gas phase. The criteria to differentiate these models depend on the gas-particle flow properties. For example, in a turbulent flow, when the particle phase volume fraction is less than 10^{-6}, the particle phase has a negligible effect on the turbulence. When the volume fraction is between 10^{-6} and 10^{-3}, the particles enhance or decay turbulence when the ratio of the particle response time to the turbulence time scale is greater or less than 1 (Elghobashi, 1994).

There are two approaches to characterize the particle field. In the two-fluid approach, both the particle and gas phases are modelled as continuum. An Eularian method is applied to develop a field description for the properties of phases. In this approach, volume averaging is used to determine the properties of each phase in the system. In turbulent flows, the equations are then time averaged to account for the turbulence (Soo, 1989). The phase interactions must be considered and expressed in continuous forms in the derived equations of both phases. For example, in a κ-ϵ-κ_p model for gas-particle turbulence flows, Zhou (1993) used the particle turbulent kinetic energy to determine the effects of gas-particle interactions on both the gas turbulence and particle velocity fluctuation. In the Lagrangian trajectory approach, the particle field is represented by particle trajectories that are acquired from integrating the particle motion equation. The gas field is described by the Eulerian method and the particle phase is

characterized by the trajectory model. There are two types of trajectory models, a deterministic trajectory model (Crowe, et al., 1977) and stochastic trajectory models (Crowe, 1991). The deterministic model neglects the turbulent fluctuation of particles, while the latter can simulate the turbulence effect on phase interactions by solving the instantaneous particle momentum equations. This approach is suitable for the cases where the particle-particle interaction is negligible, the density ratio of gas to particle is less than 10^{-3}, and particle diameter is less than the local turbulence length scale (Crowe, et al., 1996).

One important characteristic in gas-particle two-phase flows is the pressure drop to transport the gas-particle mixtures. Marcus et al (1990) investigated the pressure drop of turbulent gas-particle flows in a horizontal pipe at different superficial velocities. The results showed the pressure drop for the two-phase flows was changed compared with the pure gas flows due to the presence of particles. The pressure drop decreased in the dense flow regimes and increased in the dilute flow regimes with an increase of gas velocity. The pressure drop also increased with an increase in the particle momentum flux. The pressure drop in a two-phase flow with a higher mass flux ratio of the particles to gas was higher than that of pure gas flow (Marcus, et al., 1990). However, for the flows with the particle mass flux ratio to gas less than 2 and particle diameter less than 200 μm, the pressure drop was much less than pure gas flows (Kane, 1989). In particular, the pressure drop was decreased by 30% in a turbulent pipe flow (Boyce and Blick, 1969).

2.3 Particulate Matter Control Technologies

There are a range of different pollution control technologies for particulate matter. The type that is applied will depend on the characteristics of the particulate matter. The commercial separation equipment can be generally divided into four groups (Svarovsky, 1981) that includes aero-mechanical dry separators, aero-mechanical wet separators, electrostatic precipitators, and filters. A summary of the properties of these technologies is shown in Table 2.3. The aero-mechanical dry separators use a relative acceleration between the flow and particles to separate the phases. For example, in cyclone separators the particle centrifugal force can reach 300 to 2000 times the gravitational force (Fan and Zhu, 1998). Virtual impactors can have a high collection efficiency by turning the flow if they are well designed (Marple and Chien, 1980). The virtual impactors are reviewed later in this section together with the filtration technology that is commonly used in diesel engine exhaust.

Aero-mechanical wet separators, usually referred to as scrubbers, use liquid droplets to remove the particles. The particles are captured by the droplets mainly by inertial impaction, interception, diffusion, or by thermophoresis, diffusiophoresis, coagulation of particles, and particle growth. These type of separators typically have high efficiency and are reliable, but the particles must then be separated from the liquid phase. In addition, if the gas-solid flow include hazardous chemicals, the liquid will be harmful and thus must be treated. The particles can be charged and collected in electrostatic precipitators without flow acceleration (Chang, 2003). This technology usually requires large size to ensure higher efficiencies for a high flow rate. Auxiliary facilities are also

Table 2.3 Comparison of Particle Separation Equipment

	Aero-mechanical Dry Separator	**Aero-mechanical Wet Separator**	**Electrostatic Precipitator**	**Filter**
Separation Mechanism	Gravity (setting chambers); Centrifugal effect (cyclones, etc.)	Inertial impaction; interception; diffusion; thermophoresis, diffusiophoresis, particle coagulation and growth	Electrostatic force (external)	Inertial; interception; diffusion
System Construction	Simple	Complex	Complex	Simple
Energy Consumption	Low	Low	High	High
Cost	Low	Low	High	High
Efficiency	Usually low for small particles	High	Higher	Higher
Operation Features	Low pressure drop; more efficient for large particles	Low pressure drop; gas cooled after treatment	High-voltage power supply; low pressure drop; wide variety of exhaust	High pressure drop affecting the system
Product	Dry	Solid-liquid	Dry	Particles in filters
Application Limitation	Usually working as pre-cleaner	Not applicable for flows with harmful gaseous content; water supply required	A large size required for a high inlet flow rate;	High material strength required

needed in such equipment. Filtration technology has relatively simple designs and typically higher collection efficiency. However, with particle accumulation, there will be a large back pressure and the filters need to be regenerated as do the ESP.

2.3.1 Diesel Particle Filters

The particulate control technology widely proposed for diesel engine are diesel particle filters. The particles are captured in these filters by inertial impaction, interception, and diffusion, depending on the particle size (Mayer, et al., 1996). The fibers range in size from submicrometer to 100 μm. Diffusion is the important mechanism to collect nuclei and small accumulation-mode particles (d_p< 200 nm) but is inefficient for larger diesel particles. The collection of these modes of particles also occurs by van der Waals attraction and other forces, such as diffusiophoresis, thermophoresis, and electrostatic force (Liu, et al., 2003). Inertial impaction is effective for removing large coarse-mode particles (d_p>2,000 nm) while the interception mechanism is effective for large accumulation-mode particles (d_p > 200 nm). Both these processes become ineffective for smaller particles. Thus, there is a region in the accumulation-mode where none of the above mechanisms are most effective. The particle sizes that give minimum efficiency usually range from 50 to 500 nm (Hinds, 1982), as shown in Figure 2.5, roughly matching the accumulation mode peak for diesel exhaust.

One issue with diesel particle filters is the back pressure applied on the engine. This changes over time as filters accumulate not only particulate matter but also ash from the engine oil and fuel. The increase in the engine back pressure reduces engine power

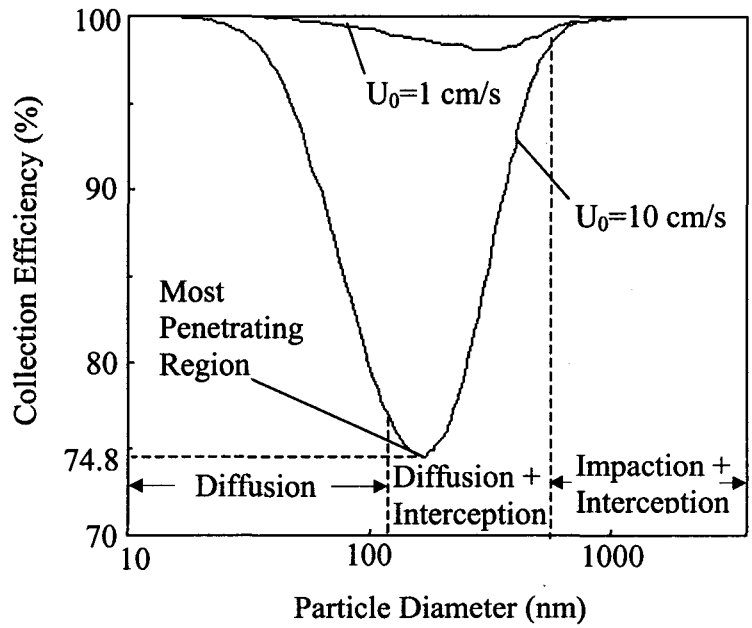

Figure 2.5 Filter efficiency as a function of particle size for face velocity of 1 and 10 cm/s, filter thickness of 1 mm and filter fiber diameter of 2 μm (Hinds, 1982)

and increases fuel consumption. It was estimated that a 100 mbar increase in filter back pressure can result in a 1 to 4.5% increase in fuel consumption (Johnson, 2003). Thus, the filter design should be based on the characteristic particle size distribution and chemical composition of each specific application (Liu, et al., 2003).

Most filters in use today are extruded wall-flow monolithic filters made of porous material, such as cordierite or silicon carbide (Miller, et al., 2002). The pressure drop in silicon carbide and cordierite filters is the sum of the losses at the inlet and outlet faces due to the plugged-cells, the inlet and outlet channel frictional losses, losses through porous wall of filter and soot layer, and the loss in the inlet expansion and exit contraction. Hashimoto et al (2002) found that without soot loading the main pressure loss were the expansion and contraction loss, while the channel flow loss and the wall flow loss were relatively minor. When the filter is loaded, the largest pressure loss was in the wall flow. The overall pressure drop typically increases with the amount of soot loading. The filtration efficiency increases with soot loading at start up, but is steady after a certain amount of soot loading. When the filtration efficiency is steady, the pressure drop increases more rapidly. The pressure drop for current Cordierite diesel filters are typically from 10 to 22 KPa at soot loading of 10 grams (Hashimoto, et al., 2002).

2.3.2 Virtual Impactors

Inertial impactors can be designed to classify particles with respect to their size. A conventional inertial impactor is shown in Figure 2.6. These devices use flow acceleration to separate particles above a certain size from the flow and deposit them on a plate, while

the smaller particles follow the flow. The particle classifiers can be operated with a series of impactors in a parallel or in a series (cascade) arrangement to classify the particles.

The performance of conventional inertial impactors were investigated by Marple and Liu (1974), Jaenicke (1974), Cheng and Yeh (1979), and Rao and Whitby (1978). The interaction of the particles with the impaction surface and particle fragmentation, bounce, or reentrainment can affect the result. In addition, the collected particles could have a chemical reaction with the impaction plate. Virtual impactors were developed to avoid such particle-surface interaction problems and are widely used in aerosol collection and separation. They operate on a similar principle except the impaction plate is replaced by a region of relatively stagnant gas contained in the cavity of a receiving probe, as shown in Figure 2.7. The flow is split into two streams, with the majority of the flow deflected while the large particles are collected in the probe. A fraction of the total flow is allowed to pass through the probe, referred to as the minor flow that contains the separated particles.

Forney et al (1982) numerically investigated the two-dimensional slit virtual impactor using a Lagrangian method and found that the internal particle loss affected the efficiency. The collection efficiency of these devices is very sensitive to the flow ratio in the two branches (Marple and Chien, 1980). In particular, the cutoff size increases as the flow ratio to the main branch increases because it changes the streamline curvature. The same is true as the Reynolds numbers of the flow changes, with higher Reynolds number flow yielding better characteristics (Marple and Chien, 1980). The geometry has a significant impact and it was recommended the entrance angle be at least 45 degree and

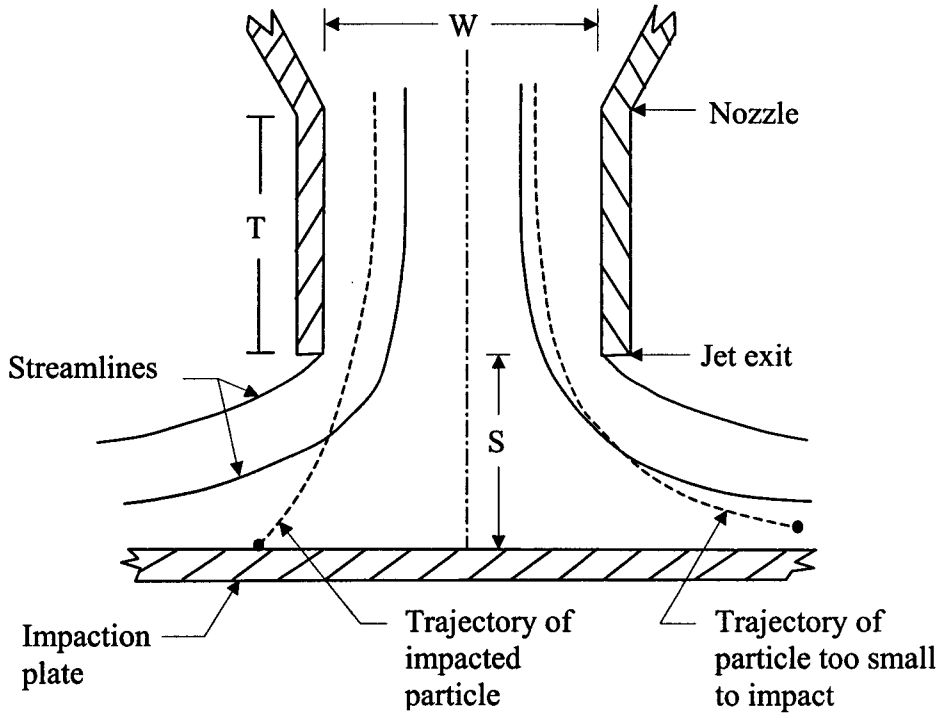

Figure 2.6 Schematic of a conventional inertial impactor (Marple, et al., 1974)

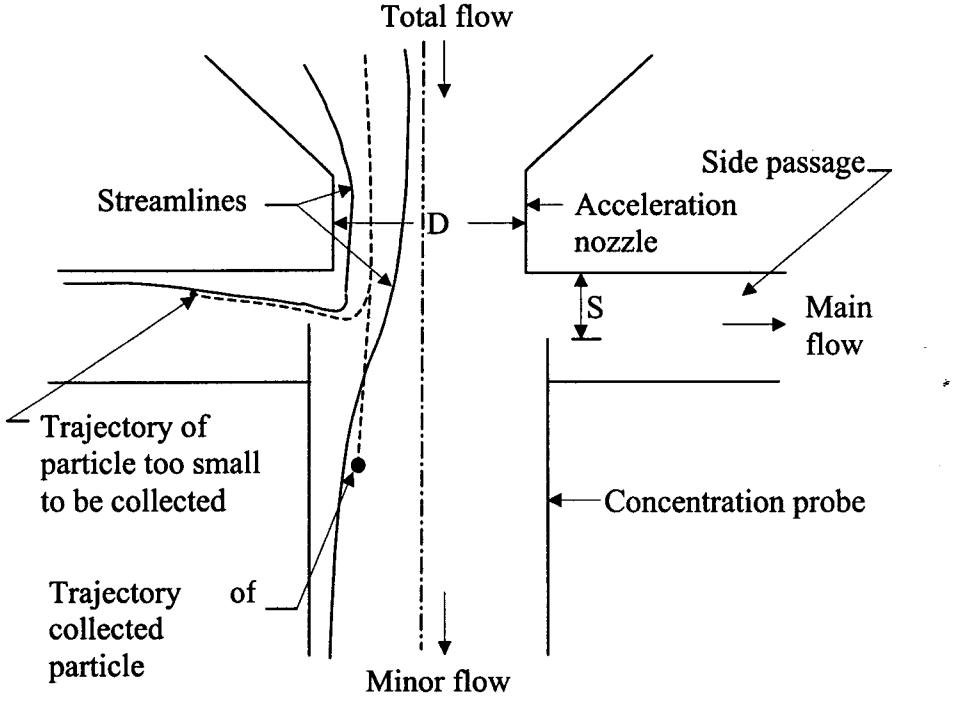

Figure 2.7 Typical model of virtual impactor (Marple, et al., 1980)

the upper edge of the concentration probe should be tapered (Marple and Chien, 1980). The collection efficiency of the virtual impactor is a function of the Stokes number given by (Fuchs, 1964)

$$St = \frac{\rho_P C V_{in} d_P^2 / 18\mu}{W/2}, \tag{2-1}$$

where ρ_P is the particle density, C is the Cunningham correction factor, V_{in} is the mean velocity at the throat, d_p is the particle diameter, μ is the fluid dynamic viscosity, W is the jet diameter for round jets and the jet width for rectangular ones.

The performance of these devices was also investigated by Barr et al. (1983), Chen and Yeh (1985), and Loo and Cork (1988). Chen and Yeh (1985) proposed a correlation for the separation efficiency and the cutoff particle size for dynamically similar virtual impactors at a fixed minor flow ratio. They noted that the device performance could be predicted when the Reynolds number is between 1,000 to 8,000, the ratio of the distance between the inlet jet and the collection probe to the inlet jet diameter is about 1, and the ratio of the collection probe diameter to the inlet jet diameter is between 1.25 and 1.5. Loo and Cork (1988) noted that round jet impactors seem to outperform rectangular ones because a high degree of flow symmetry leads to sharper cutoff and lower losses.

The design of the virtual impactor was further modified by Chen et al. (1986) and Chen et al. (1987). They introduced a clean air flow in the core of the jet that enhanced the particle separation and found the cut-out type nozzles can decrease the particle wall loss and increase the device performances greatly. Gotoh and Masuda (2001) examined

the effect of confining the aerosol flow between a core of clean air and a sheath of clean air. They noted that the annular jet type virtual impactor yielded better performance than the rectangular jet type. They observed that the end effects in a rectangular jet virtual impactor caused a three-dimensional flow structure and flow instabilities.

For a high inlet flow rate, the slit-type or multi-nozzle impactors can be used (Fang, et al., 1991). Kim et al. (2000) reported that collection efficiency decreased when the number of nozzles was increased. Sioutas et al (1994) developed a slit-shaped nozzle impactor to allow for high flow rates. For this design, the cutoff point shifted from 0.25 μm to 0.15 μm when the minor flow rate was changed from 10% to 20%. Sioutas et al (1995) designed a three-stage slit-type virtual impactor to concentrate ambient particles. For each stage, the cutoff particle size is 0.1 μm and the minor flow rate was maintained at 20% of the total flow rate.

Chapter 3 Experimental Facilities and Methodology

A prototype of a virtual impactor type flow concentrator was developed and tested on an air rig and a diesel engine exhaust test facility. The design of the concentrator is described first. The air rig used to characterize the pressure drop of the device is then presented. Finally the diesel test rig used to characterize the particulate matter separation and pressure drop across the flow concentrator is described.

3.1 Specification of the Flow Concentrator

The virtual impactor was designed in this case to function as a particle concentrator to concentrate the particulate matter in a lower flow rate minor branch as described in the previous chapter. In this case, the impactor was designed to be axisymmetric. The design of the virtual impactor is shown schematically in Figure 3.1. The incoming flow enters through a 21.18 mm (0.834") inner diameter pipe into the body of the concentrator that has an inner diameter of 34.8 mm (1.37"). The minor flow exits the concentrator through a 15.75mm (0.62") inner diameter tube so the area ratio of the concentrator is 4.9. The main flow exits the concentrator into a 154mm (6.06") diameter collection chamber. The flow then exits this chamber through two branches with inside diameter of 15.75 mm (0.62") at the end of the concentrator.

The system that was integrated into the test rigs is shown in Figure 3.2. Here, a gate valve was installed in the minor branch to control the minor flow rate so that a range

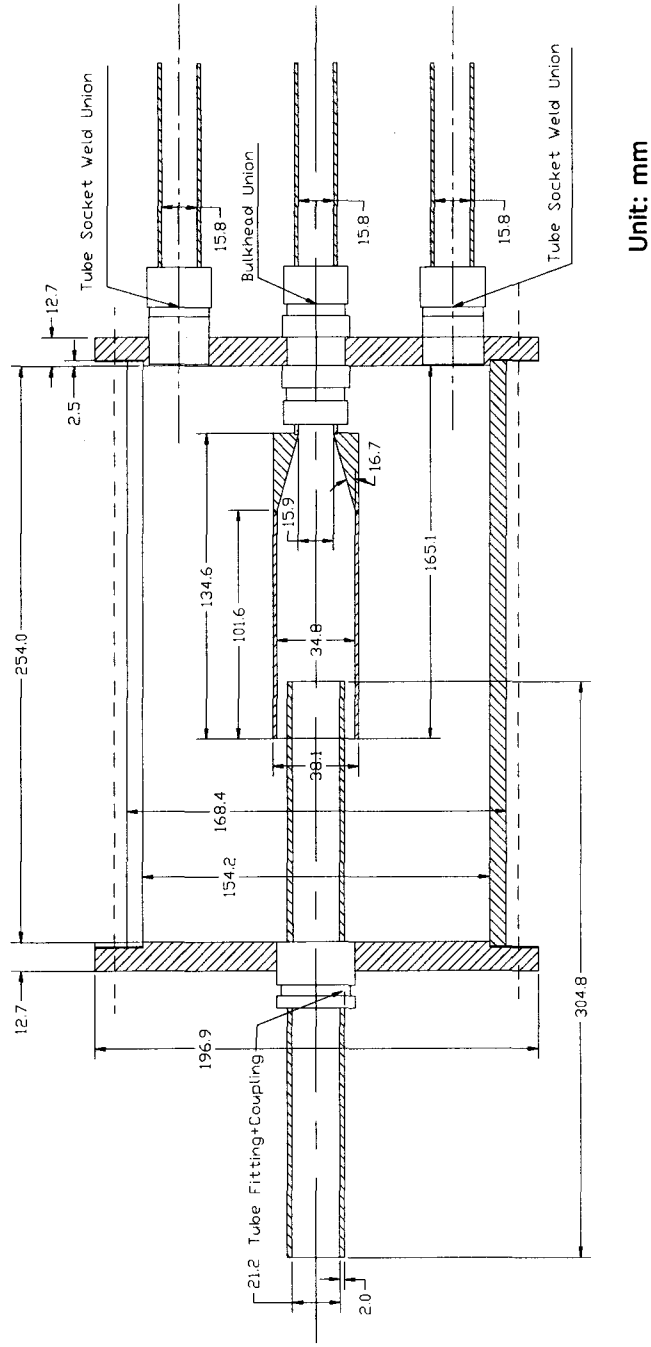

Figure 3.1 Details of the virtual impactor type flow concentrator

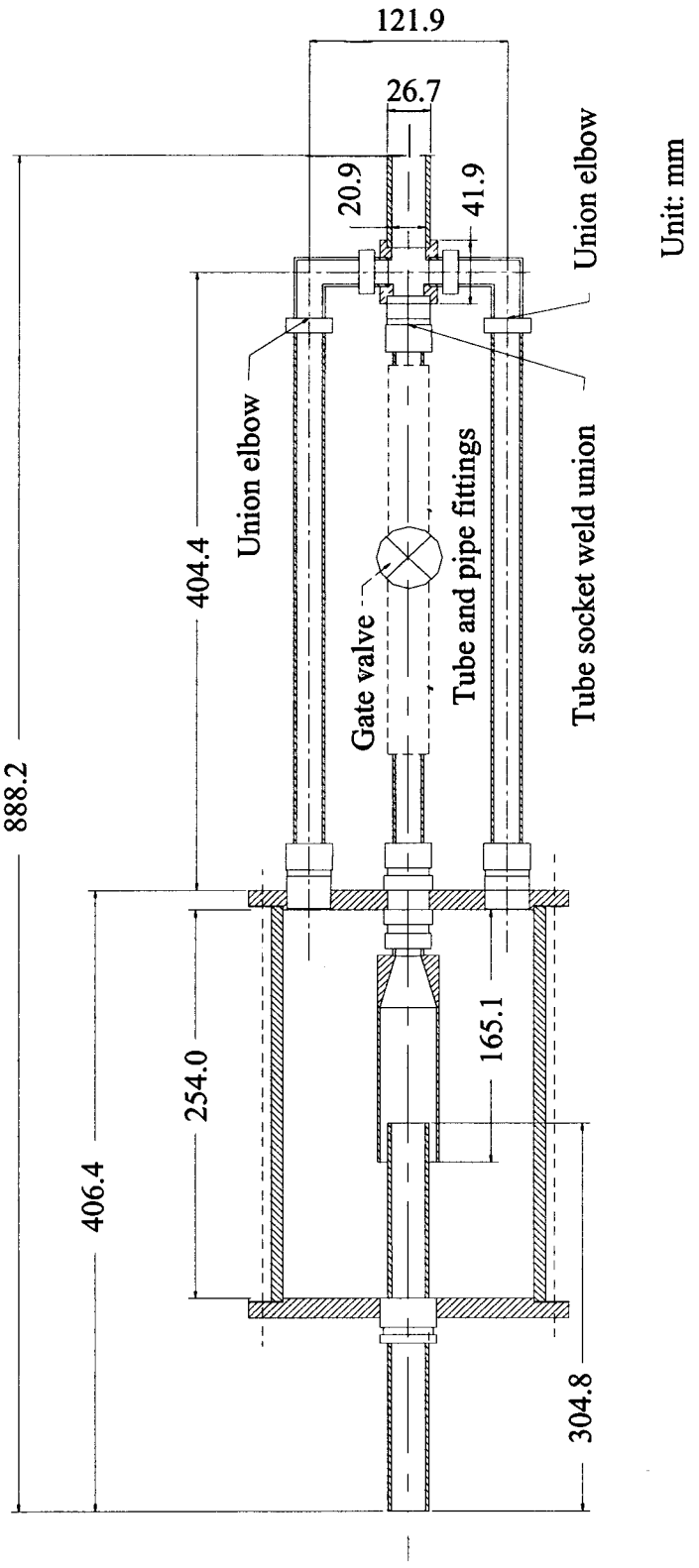

Figure 3.2 Flow concentrator system integration

of potential different external conditions can be tested. In reality, the minor branch tube would include a tube electrostatic precipitator.

The chamber was constructed from one section of 154 mm diameter stainless steel pipe with a length of 254 mm (10"). Two solid 12.7 mm thick stainless steel circular plates were fixed at the ends, with a gasket between the plates and the pipe to seal the gap. The plates were fixed using four threaded rods, equally spaced around the circumference. The inlet and outlet pipes were connected with the end plates using a pipe coupling or a bulkhead tube union as shown in Figure 3.3. The assembled concentrator was positioned on the rig using two U-shaped threaded pipe hangers. The position of the chamber was adjustable in the horizontal and the vertical directions to ensure that the pipes were aligned.

The inlet tube at the entrance of the system was held by two sets of vacuum fittings, one on the front plate and a second connected to the 35.05 mm (1.38") pipe on the rig, so the tube could be moved along the flow direction and the depth of the tube in the chamber changed. An indicator was fixed onto the tube to indicate the exact extent of the depth of the tube in the chamber.

The main branches had a length of 404 mm (15.92"), including the tube socket weld union, tubes, and tube union elbow. The minor branch construction was similar with the main branch but had a valve mounted in the line. The three branches of the flow exiting the chamber were joined downstream with a cross. The cross was fabricated for the inlet tube connections at three faces and the outlet pipe connection at one face. The outlet pipe had an inner diameter of 20.9 mm (0.82").

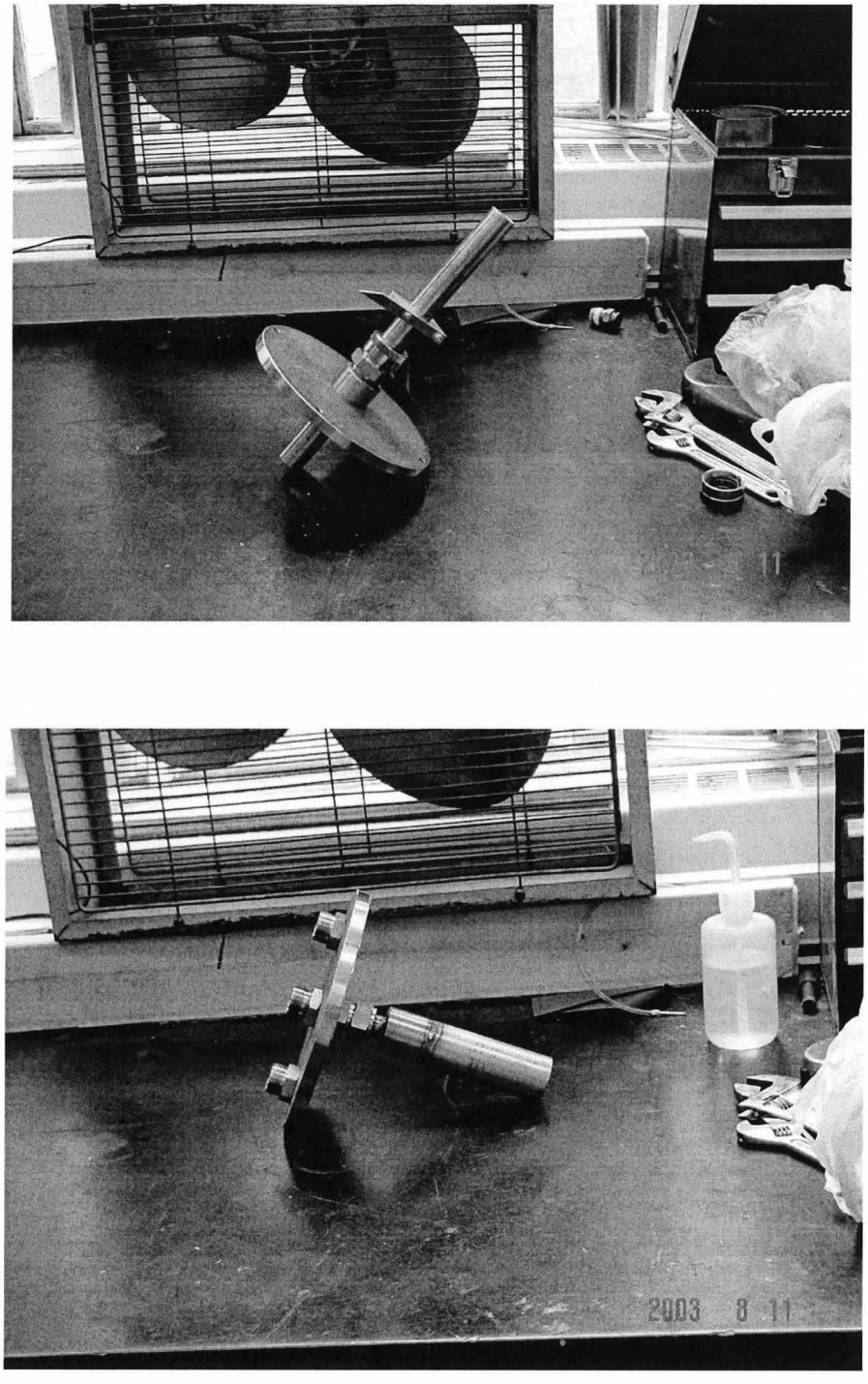

Figure 3.3 Photograph of the integrated parts at inlet and outlet of the virtual impactor

3.2 Air Test Facility

The initial tests on the flow concentrator were performed in an air test facility to determine the hydrodynamic performance of the concentrator. A schematic of the test facility is shown in Figure 3.4. The air for this facility was supplied from the laboratory compressed air line, which was regulated using a pressure regulator. The air flow passed through a flow meter and then a 7 kW air heater, where the temperature of the air could be increased. The heater was not used for these tests. The flow exited the heater through a vertical pipe with an inner diameter of 35.05mm (1.38"), and then passed through a 107 cm (42") long horizontal straight pipe section before reaching the dust flow concentrator. A rotameter was mounted in the minor branch of the flow concentrator to measure the flow rate. The outlet of the rotameter was then connected to the two main flow branches from the concentrator through a cross. The flow then exited the test facility into the ambient through a 20.9 mm (0.82") diameter pipe, a reducer, and then a 35.05mm (1.38") diameter pipe.

The pressure across the device was measured at five locations. These were at the inlet, the chamber, the minor branch, the main branch, and the outlet, as shown in Figure 3.4 and Figure 3.5. The pressure at the outlet was used as the reference point for the pressure difference calculations. The pressure difference was measured by a multi-tube manometer so the pressure difference was given by

$$\Delta P = \rho \cdot g \cdot \Delta L \cdot \sin\theta, \tag{3-1}$$

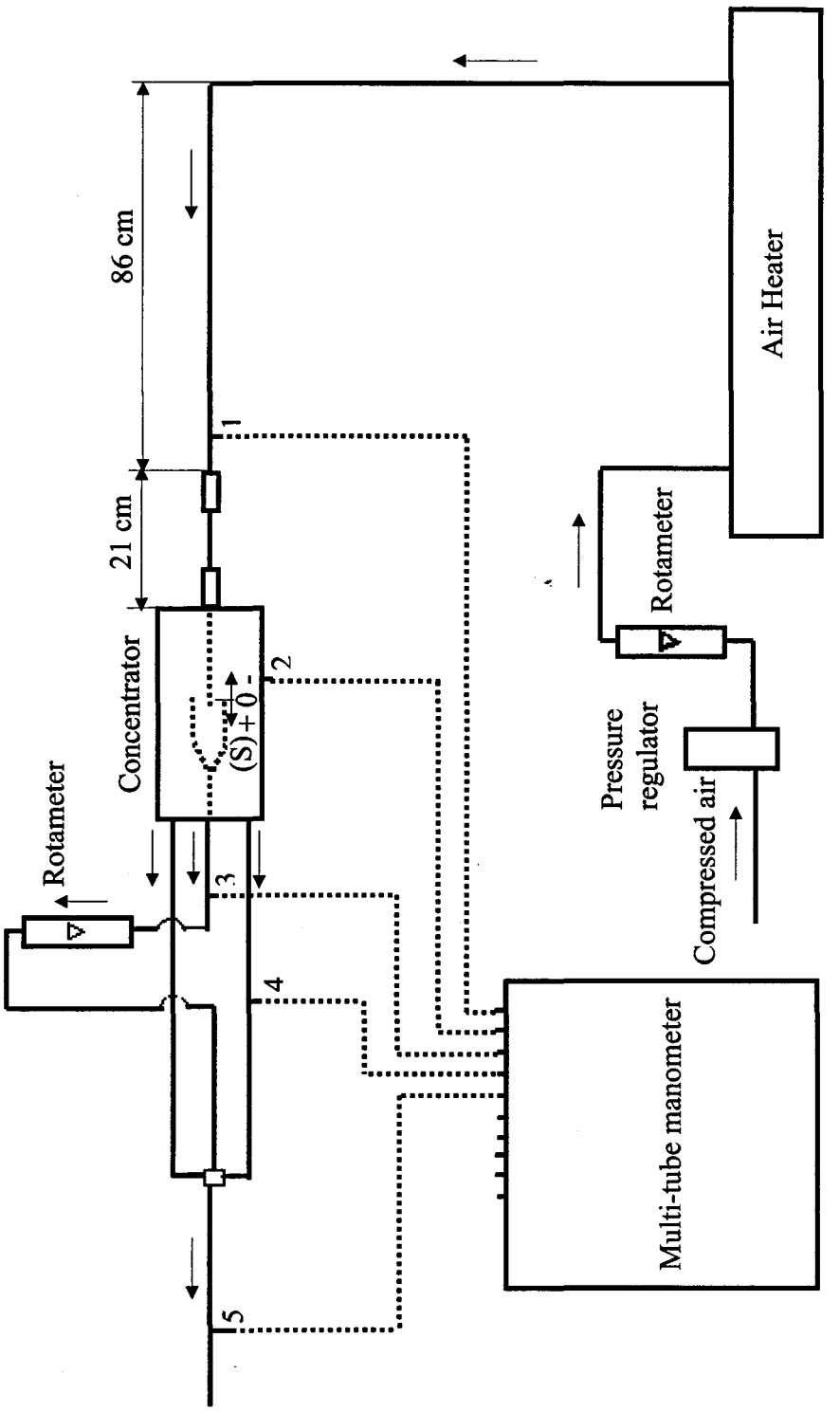

Figure 3.4 Schematic of the air test facility

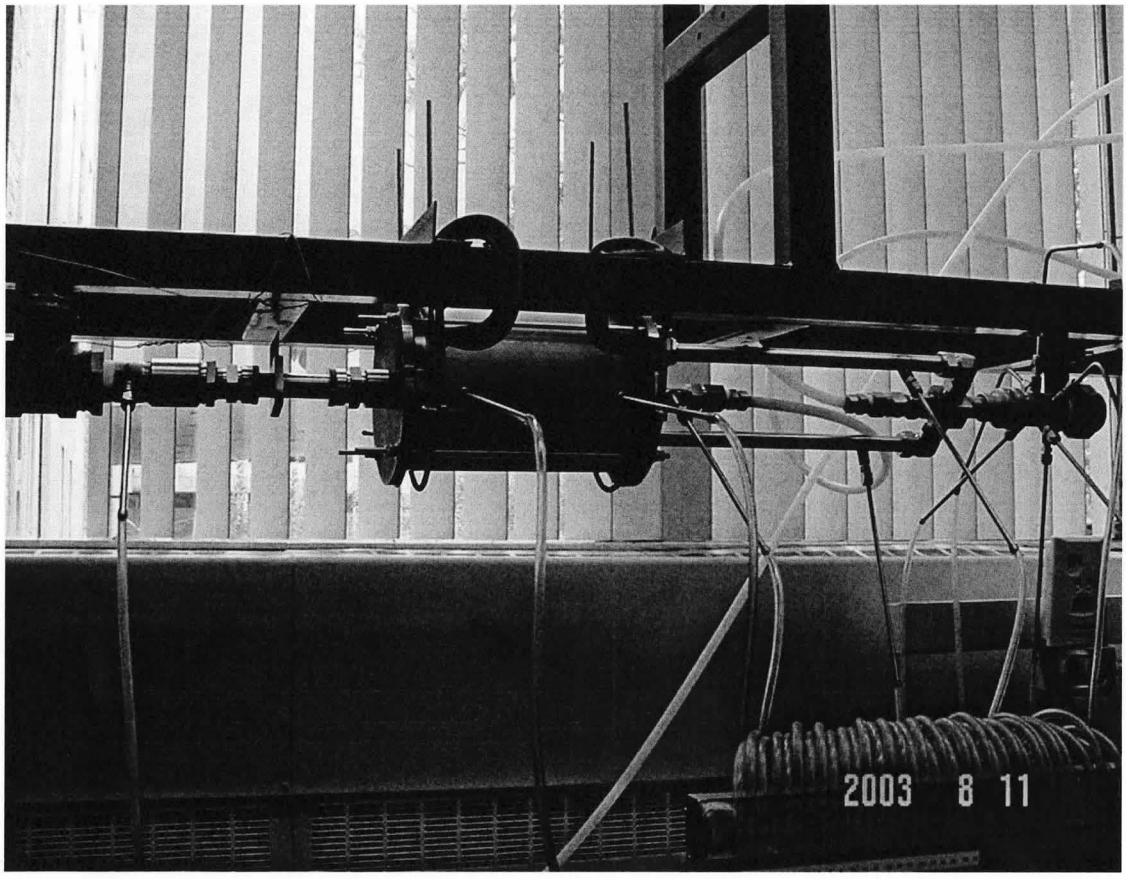

Figure 3.5 Photograph of the concentrator in the air test facility

where ΔP is the pressure difference, ρ is the density of the liquid, g is the acceleration of gravity, ΔL is the measured length of liquid column and θ is the inclination of the liquid column. The liquid in the manometer had a density of 826 kg/m^3 and the angle was from 30 degree up to 90 degree.

For the lower inlet flow rates, the flow rate was measured using a rotameter (King 7511) with a capacity up to 3.87X10^{-3} m^3/s (8.2 SCFM) and an accuracy of ±3% of full scale. The minor flow rate was measured with a Gilmont rotameter with a capacity of 2X10^{-4} m^3/s (12 LPM) and an accuracy of ±2% of full scale. For the higher inlet flow rate, the inlet flow rate was measured using a Cole-Parmer A-32462-32 rotameter with a capacity of 2.33X10^{-2} m^3/s (1400 LPM) and an accuracy of ±2% of full scale, and the minor flow rate was measured by the aforementioned King rotameter.

In these measurements, the flow rates from the rotameters were used to determine a nominal velocity given by

$$V_{in} = \frac{Q}{\pi D^2 / 4} \tag{3-2}$$

The tests were performed for air at room temperature, so the properties of the air were evaluated at a temperature of $20°C$ and a nominal pressure of 1.013X10^5 Pa. The tests were performed for air flow rates from 2.12X10^{-3} m^3/s (127 LPM) to 1.17X10^{-2} m^3/s (700 LPM) that corresponded to inlet Reynolds number from 8,500 to 46,500.

The coefficient of the pressure drop across the concentrator from the pressure measurement was determined as

$$C_p = \frac{\Delta P}{\rho \cdot V_{in}^2 / 2} \tag{3-3}$$

The normalized uncertainty of the coefficient of pressure from the pressure measurement was estimated as

$$\frac{\Delta C_P}{C_P} = \sqrt{\left(\frac{\Delta(\Delta L)}{\Delta L}\right)^2 + \left(\frac{2 \cdot \Delta Q}{Q}\right)^2 + \left(\frac{\cos\theta \cdot \Delta\theta}{\sin\theta}\right)^2} \qquad (3\text{-}4)$$

where ΔL is the uncertainty of the water column length in the manometer (± 0.2mm) , $\Delta\theta$ is the uncertainty of inclination of the manometer (± 1 degree), ΔQ is uncertainty of the rotameter reading (± $1.2X10^{-4}$ m^3/s for lower inlet flow rate and ± $4.7X10^{-4}$ m^3/s for higher flow rates). The resulting uncertainty of the coefficient of pressures was 4% to 7.2%.

3.3 Diesel Engine Exhaust Test Facility

The performance of the concentrator was also characterized using the diesel engine exhaust test facility shown in Figure 3.6. A photograph of this facility is shown in Figure 3.7. The diesel exhaust in the loop was produced by an engine generator(15LD350 Lombardini) connected to a dedicated electrical load. This one cylinder diesel engine has a displacement of 349 cm^3. The load could be adjusted from 0 to 3.4 kW. The exhaust from the engine discharges into a 35.05 mm (1.38") inner diameter pipe connected to the engine by a flexible stainless steel piping. A 0.038 m^3 (10 gallon) tank was connected to the pipe to damp flow pulsations. The exhaust flows through a vertical pipe and then was divided into two branches, one used here for the test section and the other served as a bypass. A gate valve was used to control the division of flow between the two legs. Another 0.038 m^3 tank was included in parallel with the exhaust flow to reduce the pressure fluctuations caused by the single cylinder engine. A venturi meter was installed

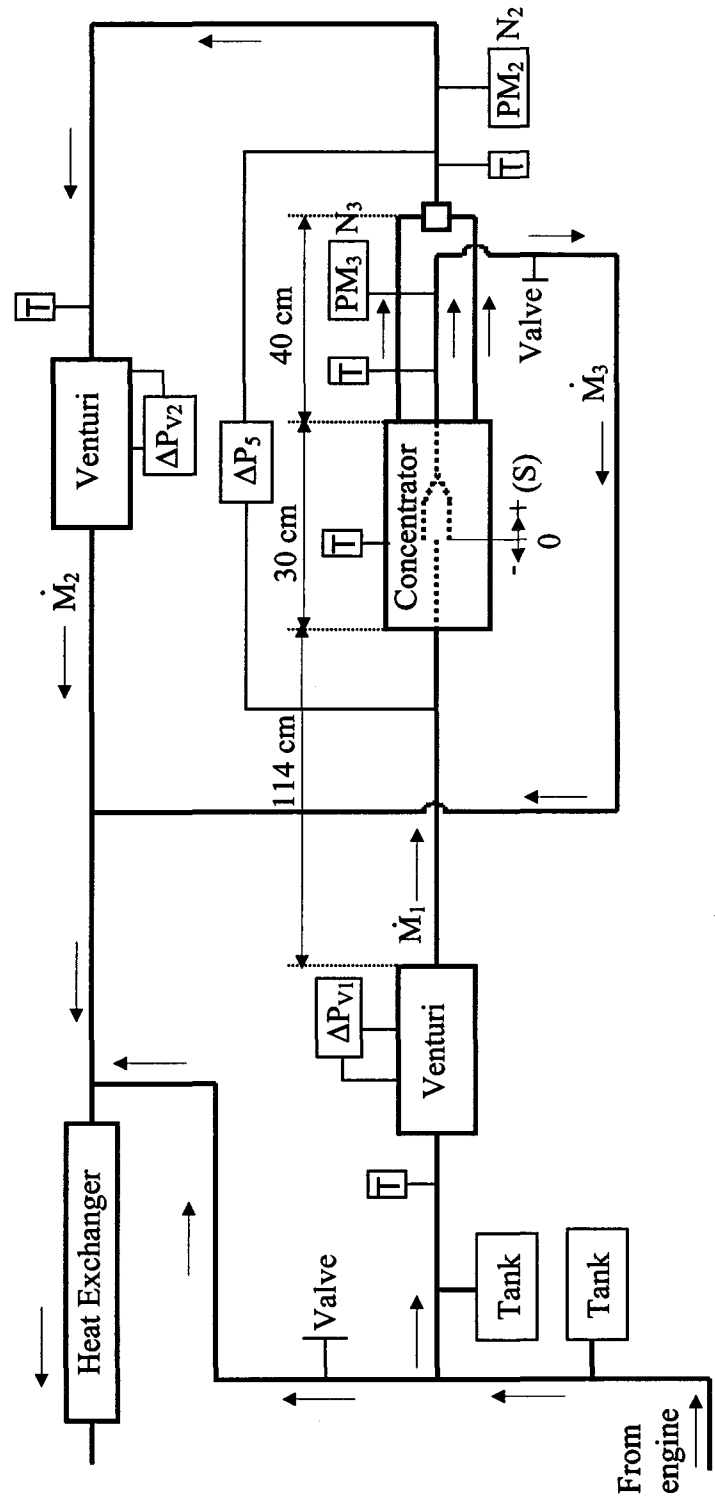

Figure 3.6 Schematic of diesel engine exhaust test facility

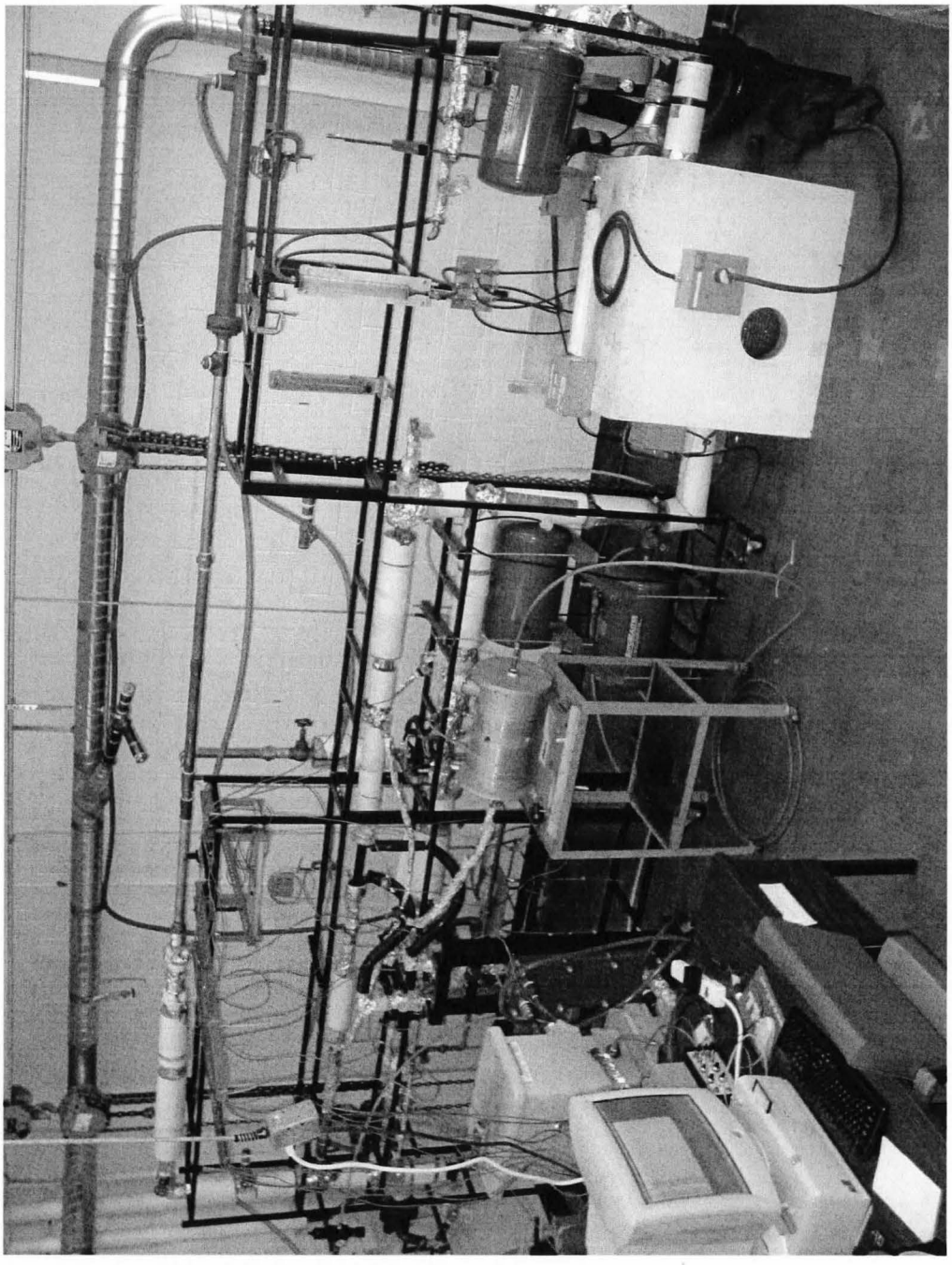

Figure 3.7 Photograph of the diesel engine test facility

upstream of the test branch to measure the total exhaust mass flow rate. A second venturi was installed downstream of the flow concentrator to measure the exhaust flow through the concentrator. The flow concentrator was installed 114 cm downstream from the point at which the exhaust flow was divided. The flow is divided into three branches at the concentrator, two main flow branches and one minor flow branch. The main flow joined at the downstream cross and then passed through the second ventrui meter. The minor branch joined the main branch downstream of the venturi meter. The by-pass leg flow joined the flow from the concentrator and the total exhaust flow passed through a heat exchanger before being discharged to the ambient.

The concentrator was mounted on the rig using threaded steel rods that were adjusted to align the concentrator with the pipe. The minor branch was connected to a 16.81 mm (0.662") diameter pipe that included a ½" gate valve that could be used to adjust the flow between the legs.

Measurements were performed to characterize the pressure drop and the particulate matter mass concentration. The performance of the system was characterized for mass flow rates of 3.1 kg/hr to 40 kg/hr that corresponded to inlet Reynolds numbers of 2,000 to 25,700. The measurements were performed for lip positions 31.75 mm (+1.25") to -15.88 mm (-0.625"). The flow rate through the minor leg was also changed by adjusting the valve in the minor branch to change the back pressure.

The pressure drop across the flow concentrator was again measured using an oil manometer. The exhaust mass flow rates of the inlet and the main flow were measured using the two venturi meters. In this case, the temperature of the exhaust gas flowing

through the venturi was measured using a T-type thermocouple located at the inlet of the venturi meter. The pressure drop across the venturi was measured using a pressure transducer (Validyne DP15TL) with a 6,900 Pa (1 PSI) diaphragm. The output of the temperature was sampled with a PCI-DAS-TC data board and the voltage output of the pressure transducer was measured with a Microstar iDSC1816 A/D board. A typical time trace of the mass flow rate at the inlet is shown in Figure 3.8 at 0 kW engine load. The mass flow rate remains constant at approximately 40 kg/hr in this case.

The particulate matter concentration in the minor and main branches of the flow concentrator was sampled using the sampling system shown in Figure 3.9. The exhaust for the minor branch was sampled using a 3.0 mm (0.118") sampling tube while the exhaust from the main branch was sampled using a 4.6mm (0.18") sampling tube. The sampling tubes were connected to a 203 mm diameter, 41 cm long sampling chamber. The particle loaded flow passed through this chamber before it was sampled by an optical particle counter (HAZDUST II Model HD-1002). As the sampled flow passed through the optical sensor head in the particle counter, the particles in the flow were detected and the particulate matter concentration were instantaneously displayed. The exhaust from each of the upstream sampling tube were drawn into the sampling chamber, one at a time. The particle counter works at a lower sampling flow rate of 1.5 to 2.3 LPM. This large chamber was used so the sampling flow rate could be achieved. The sampling tubes aligned parallel to the gas streamlines and the sampling flow rate of the exhaust gas was set so the sampling was approximately isokinetic.

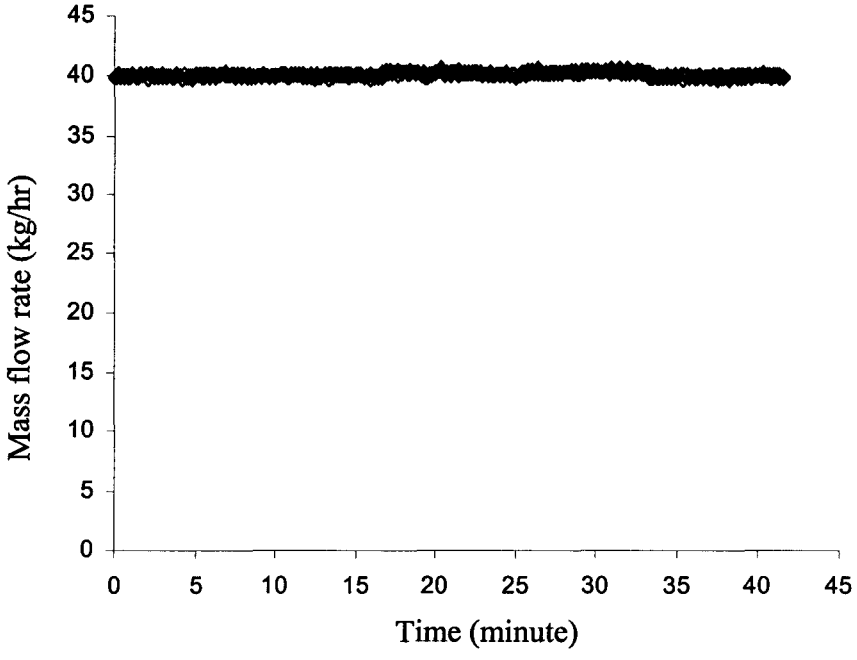

Figure 3.8 Typical time trace of inlet mass flow rate at 0 kW load

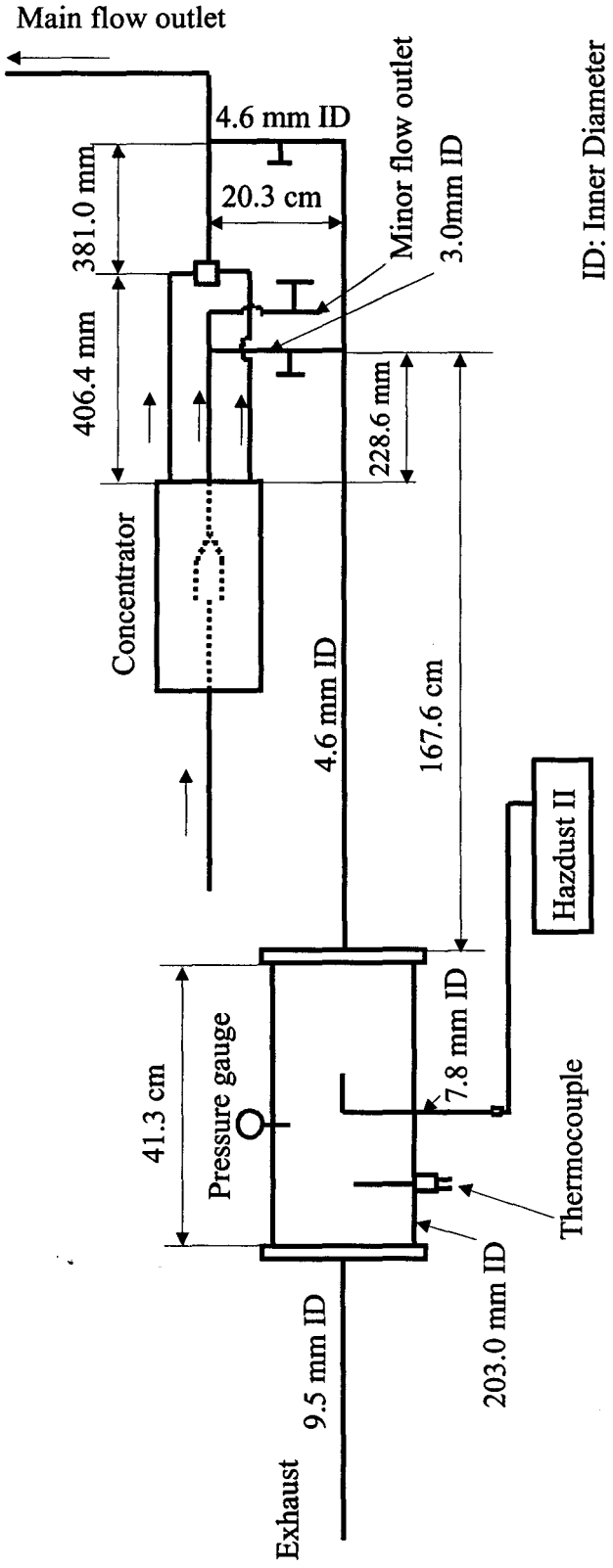

Figure 3.9 Schematic of particulate matter concentration measurement facility

A pressure gauge and a thermocouple installed in the chamber were used to monitor the pressure and temperature of the exhaust gas inside the chamber. The exhaust gas from the chamber was sampled through a 7.8 mm diameter sampling probe mounted on the chamber. This was then connected to the sampling tube of the particle counter to measure the mass concentration of the particulate matter. This instrument measures the particulate matter concentration from 0.01 to 200 mg/m^3. The maximum operating temperature of the working fluid sampled with this system cannot exceed 50 °C, so a 167.6 cm long tube was used between the chamber and the sampling tubes to reduce the temperature of the sampled exhaust flow. During the test, the PM was sampled every second, and the temperature of the sampling chamber was below 30 °C. The measurement from each leg was performed until steady readings were achieved.

Measurements of the particulate matter concentration in the main and minor branches were relatively steady throughout the tests. A typical time trace of the particulate matter concentration in the main branch is shown in Figure 3.10. The particulate matter reads a steady value after approximately one minute from the beginning of the measurement. The time trace of the particulate matter concentration in the minor branch is similar as shown in Figure 3.11.

The experiments were performed with the engine at no load. The engine was run for 30 minutes before any measurements were taken. The concentrator was characterized by setting a flow rate and testing the system for a given lip position and differenct back pressure on the minor leg. The pressure drop across the concentrator and the particulate

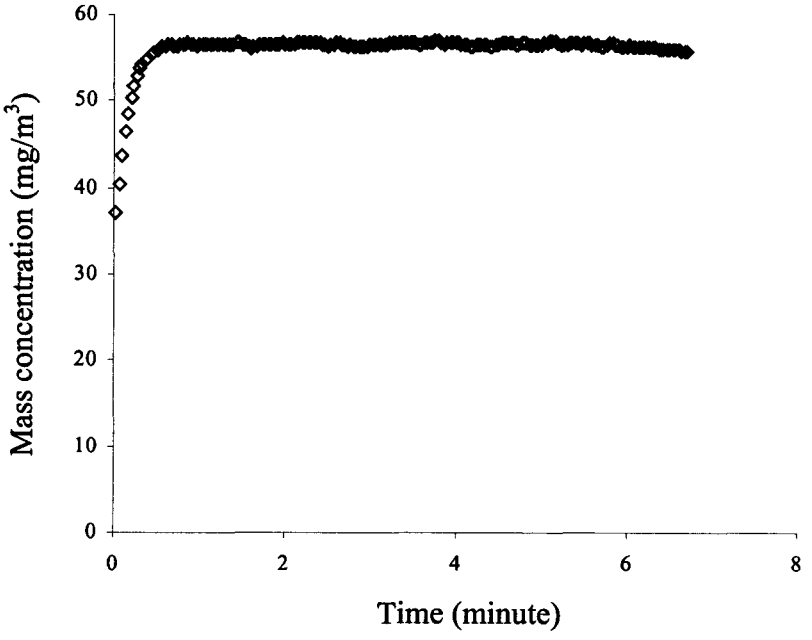

Figure 3.10 A typical time trace of PM concentration in the main branch at 0 kW load

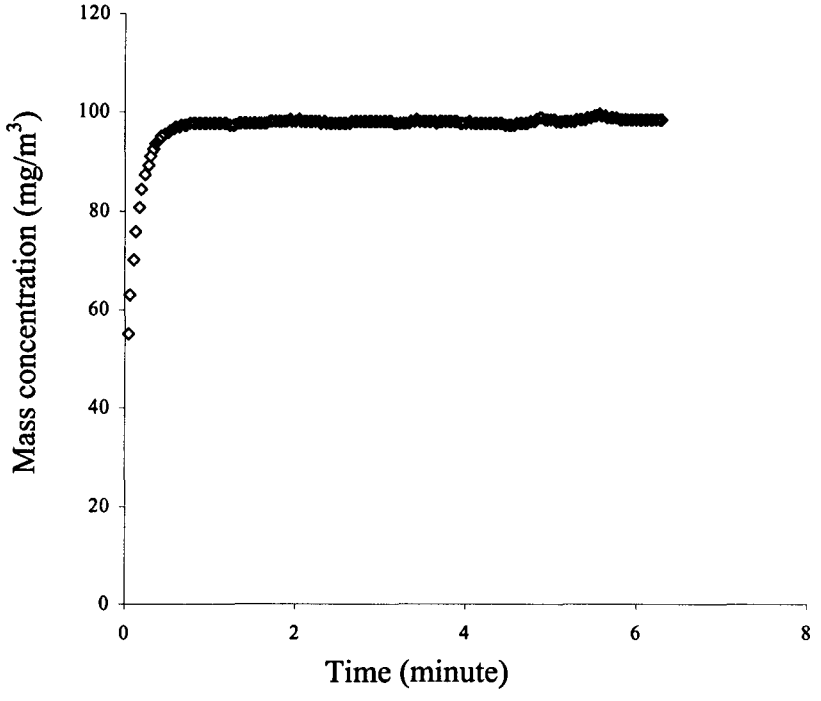

Figure 3.11 A typical time trace of PM concentration in the minor branch at 0 kW load

matter concentration in the minor and main branch were measured for each case. The tests were then repeated for other lip positions.

The particulate matter concentration ratio of the exhaust in the minor to that in the main branch was expressed by

$$R_N = \frac{N_{\text{minor}}}{N_{main}} \tag{3-5}$$

The normalized uncertainty of the concentration ratio was given by

$$\frac{\Delta R_N}{R_N} = \sqrt{\left(\frac{\Delta N_{\text{minor}}}{N_{\text{minor}}}\right)^2 + \left(\frac{\Delta N_{main}}{N_{main}}\right)^2} \tag{3-6}$$

where ΔN is the uncertainty of the concentration reading of the measurement instrument and was ± 10% of the reading. For all cases, the normalized uncertainty was ±14%.

Chapter 4 Results and Discussion

A series of experiments were performed to characterize the flow concentrator. The initial tests were performed on the air rig to obtain the pressure drop characteristics. Subsequent tests were performed in the diesel engine exhaust loop to evaluate the particulate matter separation characteristics. The tests were performed with different inlet tube lip positions. The results for the flow distribution, pressure drop, and particulate matter separation are presented and discussed in this chapter.

4.1 Pressure Drop Investigation in Air Rig Tests

In the air rig tests, the pressure drop measurements were obtained for various locations in the concentrator shown in Figure 4.1. The pressure drop coefficients across the device for different ratios of Q_{minor} to Q_{total} at a Reynolds number of 46,500 and three lip positions are shown in Figure 4.2. The ratios of Q_{minor} to Q_{total} were set equal for the three lip positions by adjusting the valve in the minor leg branch. In this case, the largest flow rate in the minor branch is 16% of the total flow rate and the pressure drop is ranged from about 12.4 to 13.5 KPa. The pressure drop across the device is relatively insensitive to the fraction of the flow traveling down the minor branch. In particular, the pressure drop decreases less than 5% when the minor flow rate is changed from 0% to 16% of the total flow rate. Similarly, the pressure drop changes at most 10% when the lip position (S/D) was changed from –0.75 to 1.5. Similar results were observed at the other Reynolds

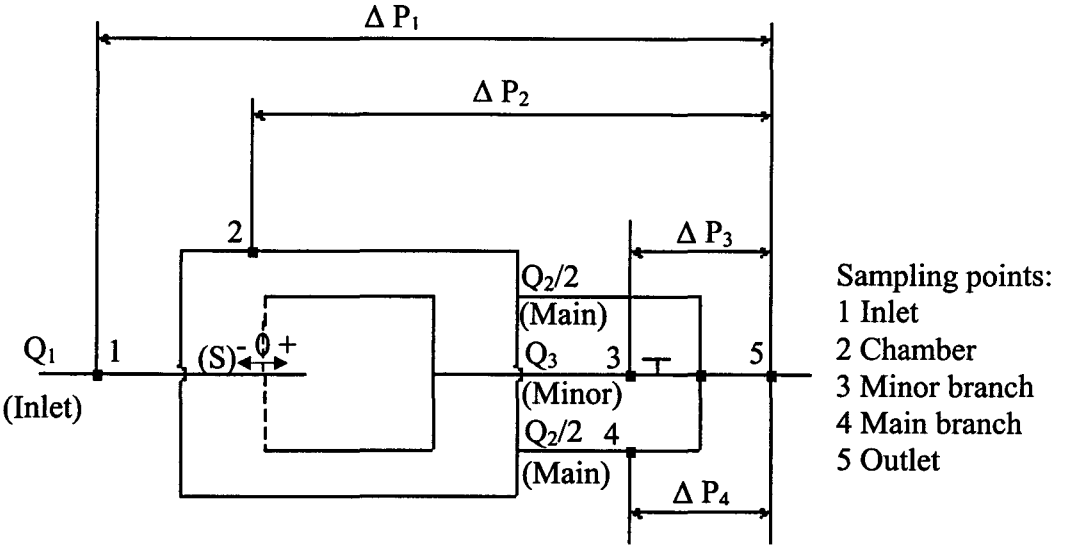

Figure 4.1 Schematic for the air test measurement

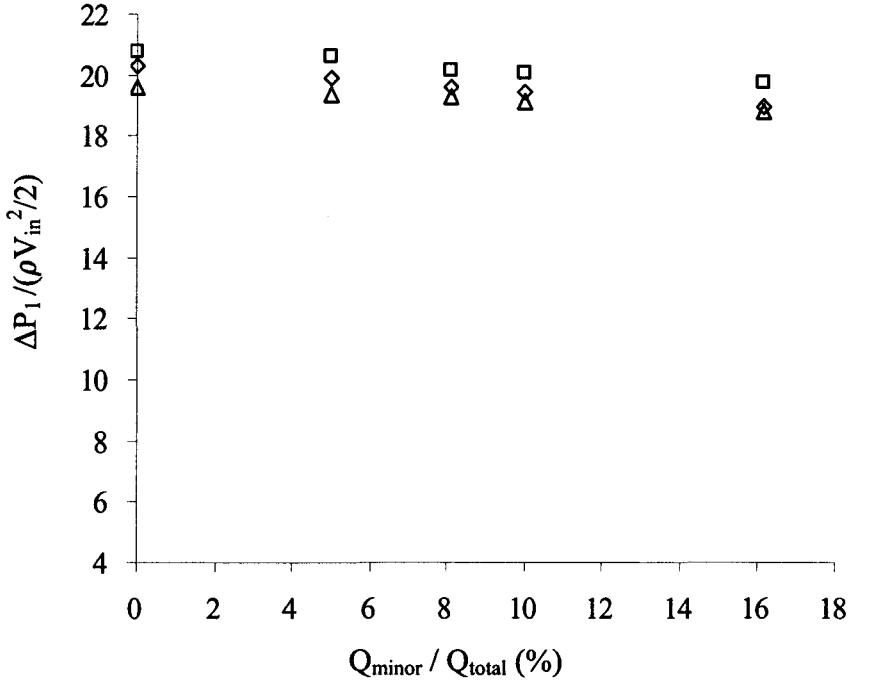

Figure 4.2 Change in pressure coefficient with minor flow ratio at a Reynolds number of 46,500 and lip positions (S/D) of △ -0.75, ◇ 0.75, □ 1.5

numbers studied. For example, the changes in the pressure coefficient with the ratio of Q_{minor} to Q_{total} for Reynolds numbers of 33,500 and 26,500 are shown in Figure 4.3 and Figure 4.4. The pressure coefficients decreased slightly with the Reynolds number and were less affected by the lip position. The maximum flow rate through the minor branch changed and the largest minor flow rates are 10% and 8% of the total flow rate respectively.

The change in overall pressure loss coefficient with Reynolds number for minor flows of 0% and 10% of the total flow are shown in Figure 4.5 and 4.6. In both cases, the pressure drop coefficient increases sharply with the Reynolds number as it exceeds 30,000. For example, as the Reynolds number is increased from 33,500 to 46,500, the pressure coefficient increase by 80%. In both cases, the pressure drop was higher when the lip was further in the concentrator but the influence of the lip positions on the pressure drop coefficient is surprisingly small, especially at a higher Reynolds number. For example, the increase in pressure coefficient was only 3% as the lip position was changed from –0.75 to 1.5 for the Reynolds number ranged from 33,500 to 46,500. The change in the pressure loss coefficient with Reynolds number for lip position (S/D) of 0.75 is shown in Figure 4.7 for minor flow rates of 0%, 5%, and 10% of the total flow rate. The pressure loss coefficient decreases as the minor flow is increased. For example, when the minor flow rate was changed from 0% to 10% of the total flow rate, the pressure loss coefficient decreased by 10%. The change in the pressure loss coefficient is less at the higher Reynolds numbers. Similar results were found for the three lip positions. For example, the results for the lip position of –0.75 (Figure 4.8) show the influence of the flow ratio to the

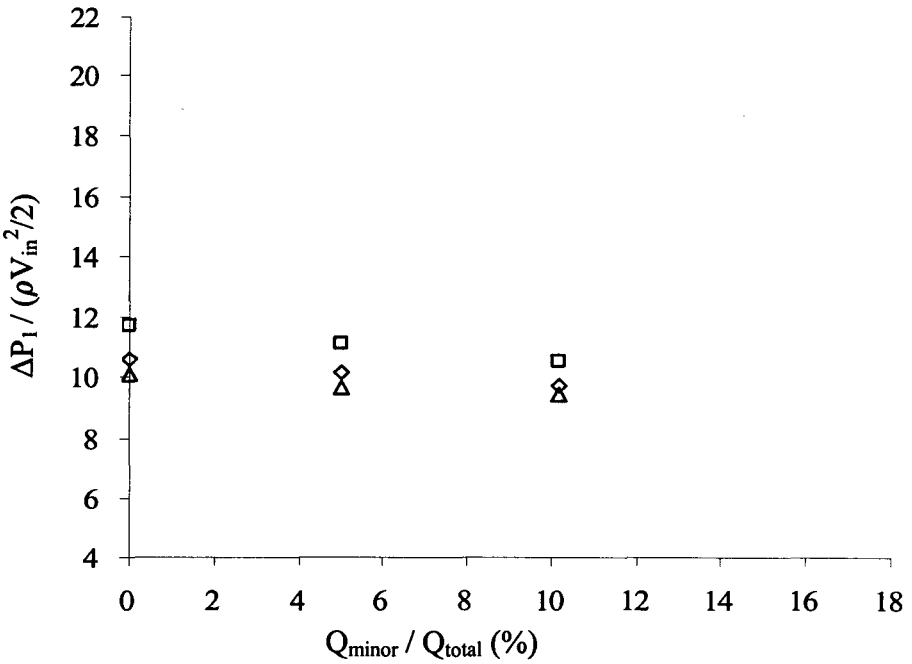

Figure 4.3 Change in pressure coefficient with minor flow ratio at a Reynolds number of 33,500 and lip positions (S/D) of △ -0.75, ◇ 0.75, □ 1.5

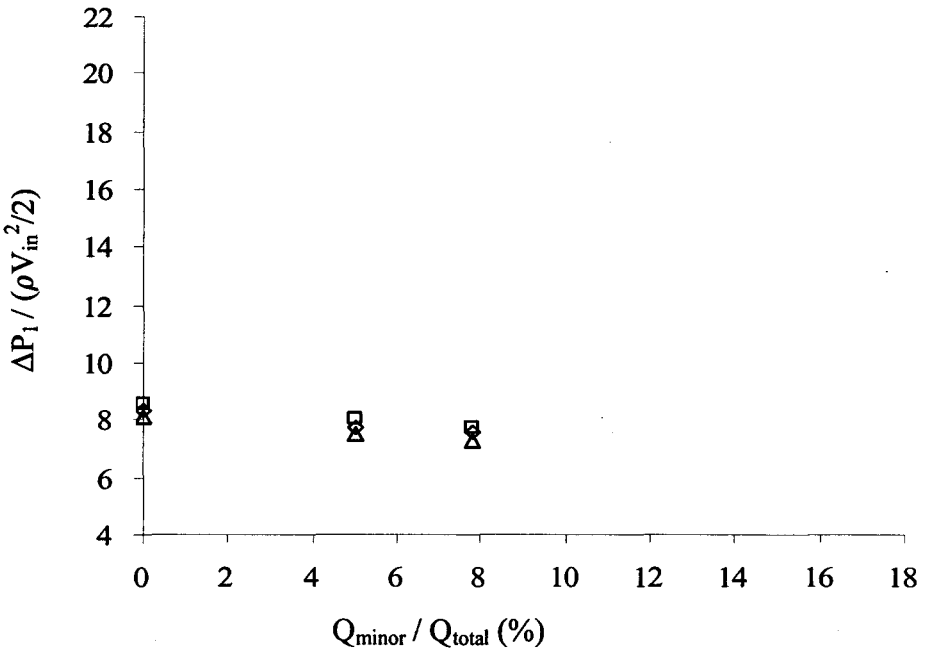

Figure 4.4 Change in pressure coefficient with minor flow ratio at a Reynolds number of 26,500 and lip positions (S/D) of △ -0.75, ◇ 0.75, □ 1.5

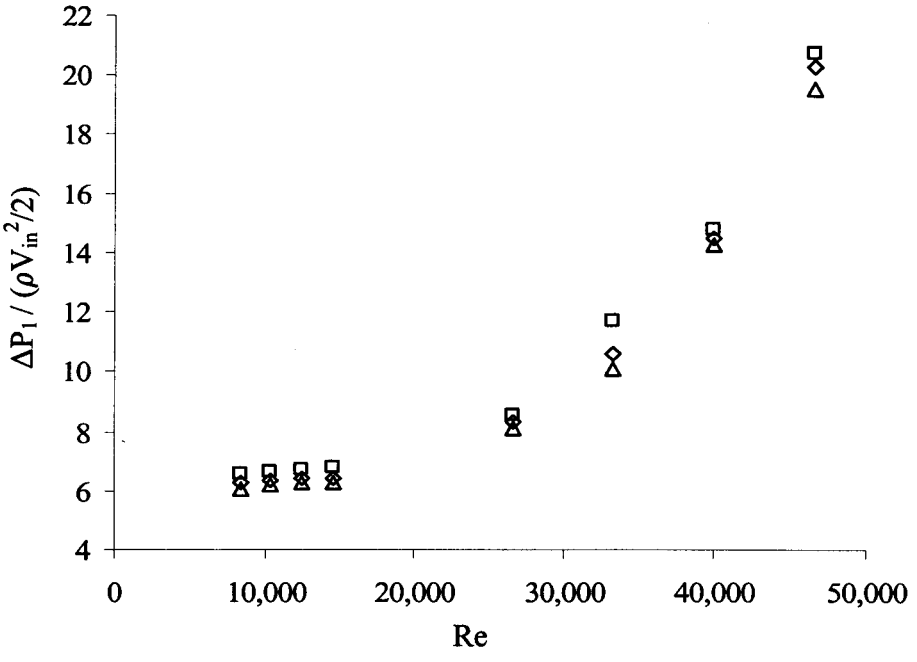

Figure 4.5 Change in pressure coefficient with inlet Reynolds number at a minor flow ratio 0% and lip positions (S/D) of △ -0.75, ◇ 0.75, □ 1.5

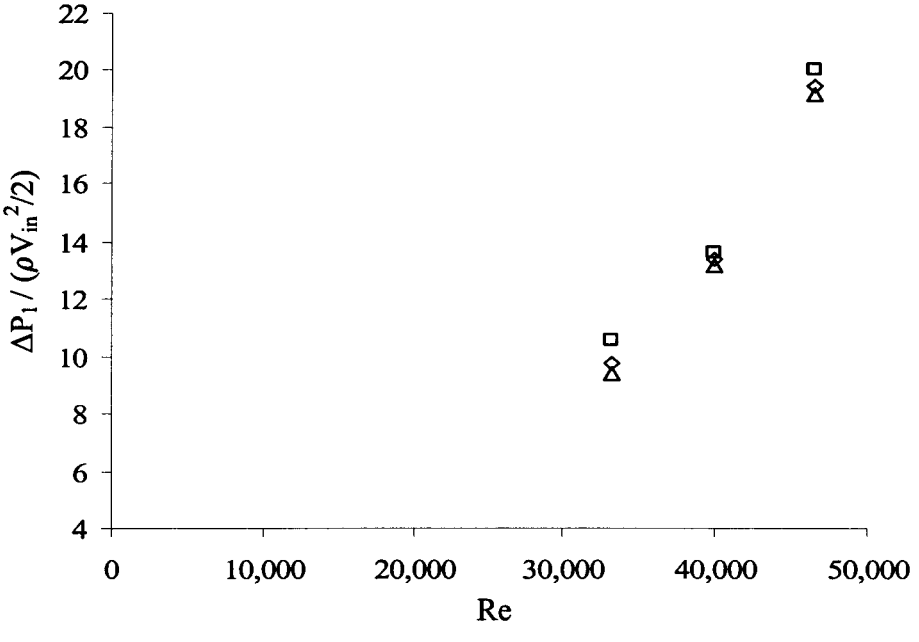

Figure 4.6 Change in pressure coefficient with inlet Reynolds number at a minor flow ratio 10% and lip positions (S/D) of △ -0.75, ◇ 0.75, □ 1.5

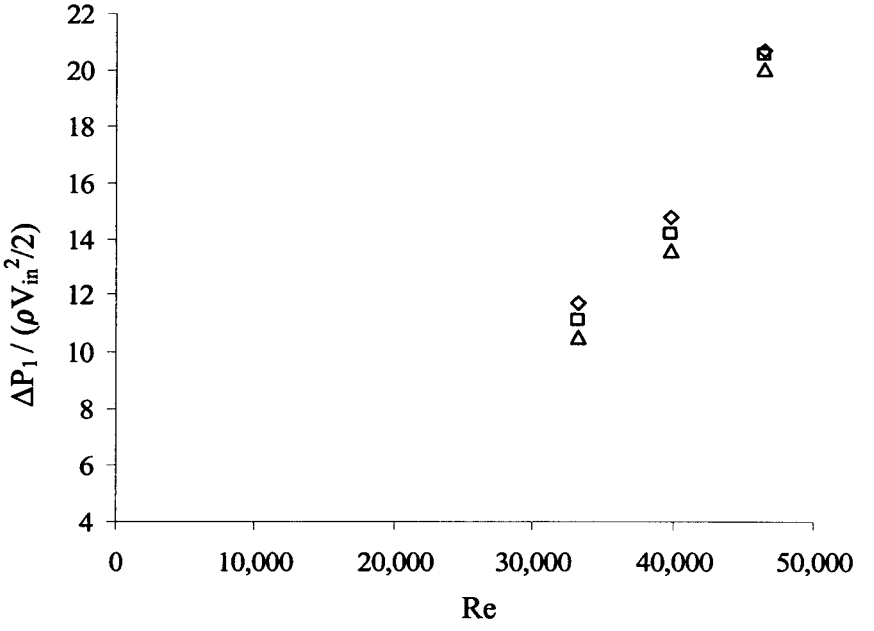

Figure 4.7 Change in pressure coefficients with inlet Reynolds numbers at a lip position of 0.75 and minor flow rates: ◇ 0%, □ 5%, △ 10% of the total flow rate

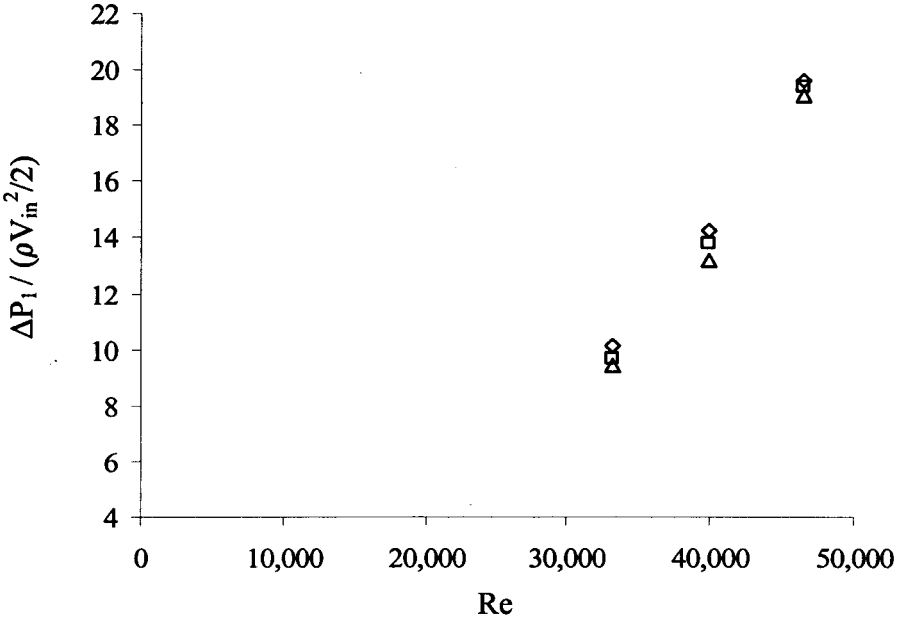

Figure 4.8 Change in pressure coefficients with inlet Reynolds numbers at a lip position of -0.75 and minor flow rates: ◇ 0%, □ 5%, △ 10% of the total flow rate

minor branch was much smaller.

The effect of the inlet Reynolds number on the pressure loss distribution among the sections of the device was further investigated for three Reynolds numbers at a lip position of -0.75 as shown in Table 4.1. The minor flow ratio to the total was set 0% so the total flow passed through main outlet after passing through the concentration probe and the chamber. The sectional pressure loss coefficients increase with an increase in the Reynolds number. For example, when the Reynolds number increased from 14,700 to 40,000, the overall and sectional pressure coefficients increased sharply. The distribution of the pressure loss in the individual sections to the total showed the pressure drop between the chamber and the outlet was 70% of the total pressure loss and the pressure loss between the inlet and the chamber was 30% for the three Reynolds numbers. Similar results were found when the minor to total flow ratio was 10% as shown in Table 4.2. For the minor flow, 95% of the total pressure drop occurred from the minor branch to the outlet due to the large resistance caused by the valve used to control the flow in the minor branch. For the main flow, the pressure drop from the inlet to the chamber is 30% of the total pressure drop and the pressure drop from the chamber to the outlet is 70% of the total pressure drop. It indicates that the pressure loss mainly occurs from the chamber to the outlet, or outside of the concentrator region. In this design, there is a sudden expansion as the flow exits the concentration probe into the chamber and a sharp flow area contraction between the chamber and the main flow branch that caused losses. There is also a sharp change in flow direction at the cross where the two main branches joined that caused a significant loss. The aforementioned losses become significant when the

Table 4.1 Sectional pressure drop coefficients distribution and the fractional ratios for the sections of 1-3 inlet to minor; 3-2 minor to chamber; 2-4 chamber to main; 4-5 main to outlet with lip position of –0.75 and minor to total flow ratio of 0%

	Sectional pressure drop coefficient				
Re	$C_{p\,1\text{-}3}$	$C_{p\,3\text{-}2}$	$C_{p\,2\text{-}4}$	$C_{p\,4\text{-}5}$	$C_{p\,1\text{-}5}$
8,500	0.32	1.37	1.95	2.44	6.08
14,700	0.42	1.44	1.98	2.46	6.30
40,000	0.86	3.20	4.51	5.96	14.53
	Ratio of sectional pressure loss to the total				
Re	$\Delta P_{1\text{-}3}/\Delta P_{1\text{-}5}$	$\Delta P_{3\text{-}2}/\Delta P_{1\text{-}5}$	$\Delta P_{2\text{-}4}/\Delta P_{1\text{-}5}$	$\Delta P_{4\text{-}5}/\Delta P_{1\text{-}5}$	$\Delta P_{1\text{-}5}/\Delta P_{1\text{-}5}$
8,500	5%	23%	32%	40%	100%
14,700	7%	23%	31%	39%	100%
40,000	6%	22%	31%	41%	100%

Table 4.2 Sectional pressure drop coefficients distribution and the fractional ratios for the sections of 1-3 inlet to minor; 3-2 minor to chamber; 2-4 chamber to main; 4-5 main to outlet with lip position of –0.75 and minor to total flow ratio of 10%

	Sectional pressure drop coefficient				
Re	$C_{p\,1\text{-}3}$	$C_{p\,3\text{-}2}$	$C_{p\,2\text{-}4}$	$C_{p\,4\text{-}5}$	$C_{p\,1\text{-}5}$
33,500	0.57	2.07	2.92	3.87	9.43
40,000	0.66	3.03	4.22	5.27	13.18
46,500	0.96	4.58	5.93	7.65	19.12
	Ratio of sectional pressure loss to the total				
Re	$\Delta P_{1\text{-}3}/\Delta P_{1\text{-}5}$	$\Delta P_{3\text{-}2}/\Delta P_{1\text{-}5}$	$\Delta P_{2\text{-}4}/\Delta P_{1\text{-}5}$	$\Delta P_{4\text{-}5}/\Delta P_{1\text{-}5}$	$\Delta P_{1\text{-}5}/\Delta P_{1\text{-}5}$
33,500	6%	22%	31%	41%	100%
40,000	5%	23%	32%	40%	100%
46,500	5%	24%	31%	40%	100%

Reynolds number is increased. Thus further optimization of the design presented in chapter 7 could likely reduce the overall pressure drop.

4.2 Diesel Engine Exhaust Test Results

The pressure drop and particulate matter separation of the flow concentrator was characterized using the diesel engine exhaust test facility described in chapter 3. The measurement location for the pressure drop and particulate matter are shown schematically in Figure 4.9. The change in the pressure drop coefficient with the flow rate in the minor branch for inlet flow Reynolds numbers from 2,200 to 25,700 are shown in Figure 4.10, 4.11 and 4.12. The ratio of flow in the minor branch to the total flow rate was up to 30% and is higher than that in the air tests. In all cases, the pressure loss coefficient decreased as the fraction of the flow rate through the minor branch was increased. The pressure loss coefficient was increased as the inlet tube was placed deeper in the concentration probe. The ratio of the mass flow in the minor branch to the total mass flow rate $\dot{M}_{minor} / \dot{M}_{total}$ had a more significant influence on the pressure coefficient than the lip position. The changes caused by the lip positions were below 15%, while the coefficients decreased by 40% as the ratio of $\dot{M}_{minor} / \dot{M}_{total}$ increased from 0% to the maximum value of 30%.

For the case with inlet Reynolds number of 25,700, the decrease in pressure coefficient when the minor flow rate changed from 0% to 8% of the total flow rate is about 20% and is larger than that of the clean air tests at the corresponding Reynolds number. The lip position had a more significant influence on the pressure drop coefficient

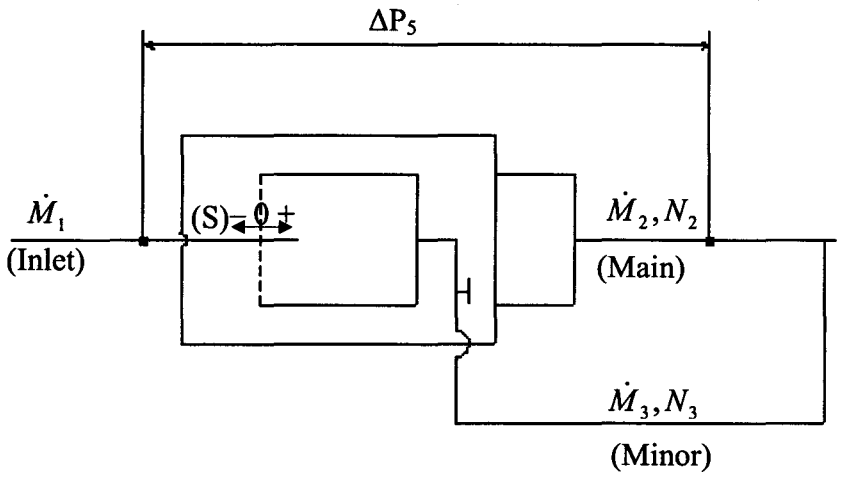

Figure 4.9 Schematic of engine test measurement

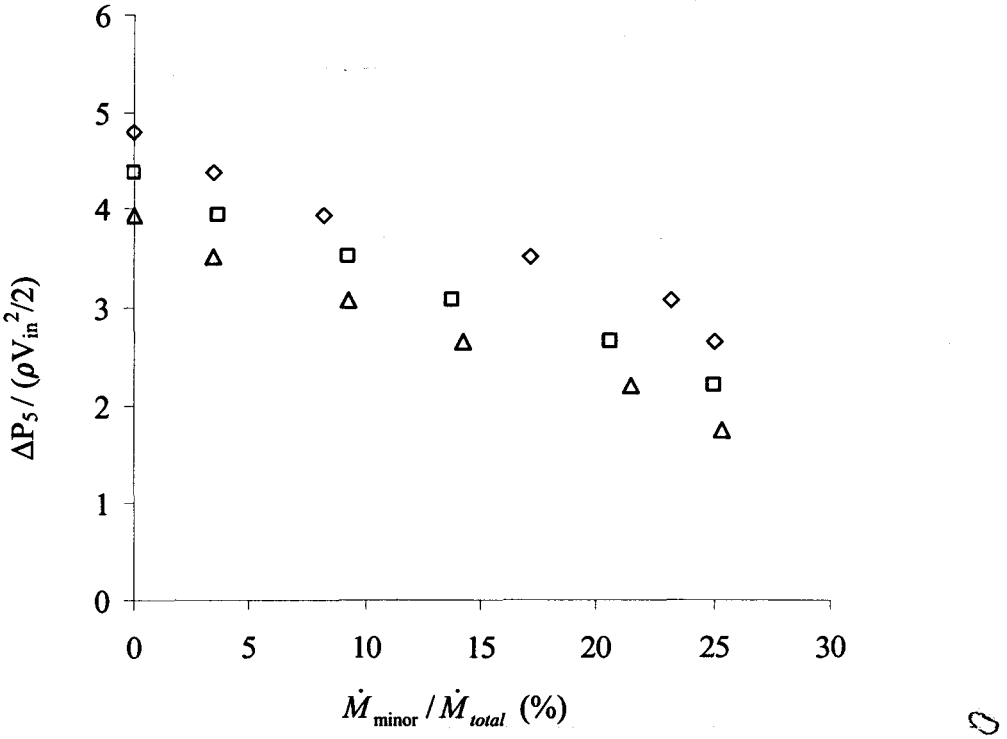

Figure 4.10 Change in pressure coefficient with minor flow ratio at a Reynolds number of 2,200 and lip positions (S/D) of △ -0.75, □ 0.75, ◇ 1.5

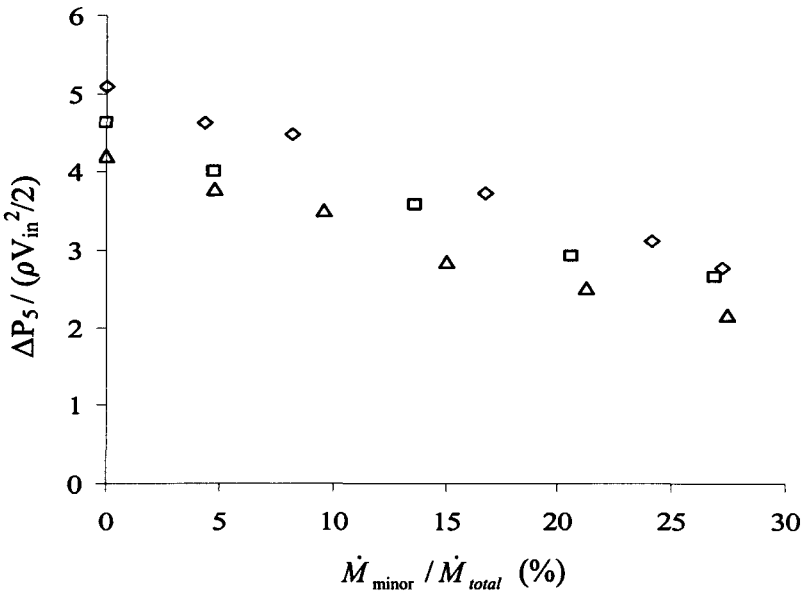

Figure 4.11 Change in pressure coefficient with minor flow ratio at a Reynolds number of 14,000 and lip positions (S/D) of △ -0.75, □ 0.75, ◇ 1.5

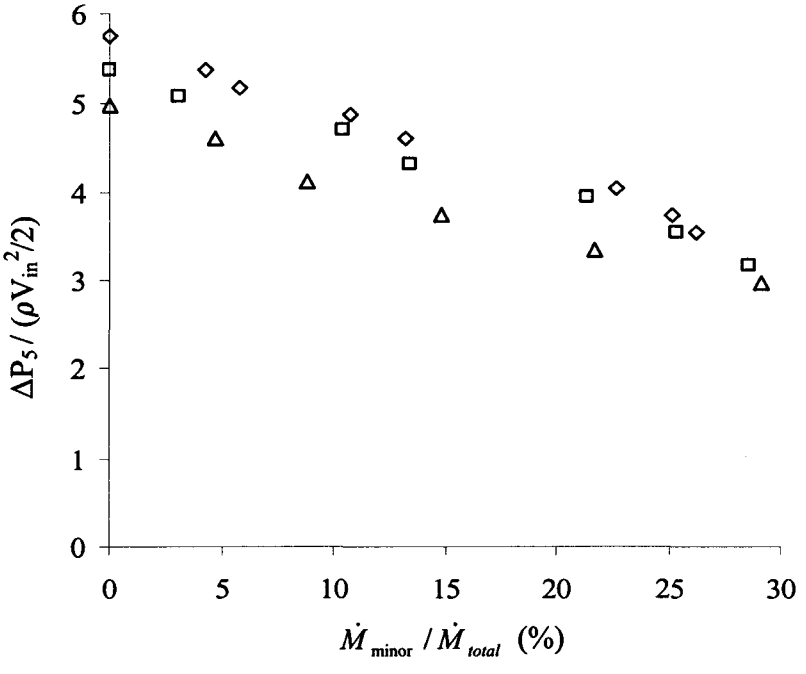

Figure 4.12 Change in pressure coefficient with minor flow ratio at a Reynolds number of 25,700 and lip positions (S/D) of △ -0.75, □ 0.75, ◇ 1.5

than that in the air test. For example, the increase in pressure coefficient when the lip position (S/D) changed from –0.75 to 1.5 is 14% while the increase is only 5% in the clean air test. In addition, the pressure loss coefficients in the engine tests were compared to those from the air tests at each lip position and minor flow ratio as shown in Table 4.3. It was found that the pressure loss coefficients in the engine tests were much less than those in the corresponding air tests. For example, at a Reynolds number of about 26,000, the pressure loss coefficient in the engine tests for the lip position of –0.75 and minor flow ratio of 0% is 38% less than that in the air tests. Similar results were found for the case with inlet Reynolds number of about 14,000.

The aforementioned difference between the air rig tests and the engine exhaust tests could be caused by the differences in the working fluid properties. In the air rig, the fluid is air while in the engine rig, the fluid is a two-phase mixture of gas and particulate matter. The gas flow field can be significantly affected by the presence of particulate matter through turbulence modulation. When the particles are dispersed in the dilute turbulent gas flow, the interaction between the two phases increases the dissipation energy and the production of energy for the gas phase. The increase in kinetic energy dissipation due to the work performed by the gas phase on the particles leads to turbulence reduction, while the increase in energy production due to the wake of the particles leads to turbulence enhancement. For small particles ($S_t << 1$), the particle velocity approaches the gas velocity and the turbulence intensity is attenuated. The turbulent viscosity of the gas phase is also reduced (Fan and Zhu, 1998), resulting in a decrease in wall friction. The pressure drop across the system was balanced by the wall

Table 4.3 Comparison of the results in air tests with inlet Reynolds number of 26,500 and engine tests with inlet Reynolds number of 25,700

Lip position (S/D)	Minor to total flow ratio (%)		Pressure drop coefficient	
	Air tests	Engine tests	Air tests	Engine tests
-0.75	0	0	8.10	5.01
	5	4.8	7.47	4.62
	8	8.8	7.24	4.13
0.75	0	0	8.36	5.37
	5	3.5	7.74	5.13
	8	10.2	7.56	4.73
1.5	0	0	8.58	5.76
	5	4.4	8.06	5.42
	8	10	7.75	4.91

friction and the changes in the momentum flux of the two phases. In particular, the velocity profile of the two phases can be influenced by the deposition and agglomeration of the particles near the wall region, and hence change the wall friction.

The measured pressure drop results from the engine tests for the inlet Reynolds number of 2,200 are compared to the flow simulation results in Table 4.4. In the numerical simulations, the pressure difference was between the inlet and the main flow branch. In the engine tests, the measured pressure difference was between the inlet and the chamber. The maximum flow rate of the minor branch was 25% of the total flow in the tests. In the numerical simulations, only the case with a minor outlet to inlet diameter ratio of 0.1 yielded minor flow ratios close to this value (Figure A.14). The pressure coefficients for the engine tests and the simulations are compared for lip positions of 1.5, 0.75, and –0.75. The results from the engine tests are in reasonable agreement with the simulation, with the variation in pressure loss coefficient for each lip position less than 10%.

The change of the particulate matter concentration ratio of the minor flow to the main flow with $\dot{M}_{minor} / \dot{M}_{total}$ for the different lip positions are shown in Figure 4.13, 4.14 and 4.15. The ratio of minor flow to main flow ranged from 5% to 30% for all three cases. For the lip position (S/D) of 1.5, the variation of the concentration ratio is similar at all three Reynolds numbers. The concentration ratio increases with the flow ratio and reach a maximum at minor to total flow ratio of approximately 25%. The concentration ratio decreases sharply beyond this optimum flow ratio. The value of $\dot{M}_{minor} / \dot{M}_{total}$ at which the maximum concentration occurs changed to 13% and 15% for the lip positions

Table 4.4 Comparison of the results in simulation and engine tests

	Lip position (S/D)	**Inlet Reynolds number**	**Flow ratio of the minor to total**	**Pressure loss coefficient**
Simulations	1.5	2,014	28%	0.96
	0.75	2,076	25%	0.72
	-0.75	2,138	20%	0.48
Engine tests	1.5	2,200	25%	0.84
	0.75	2,200	25%	0.69
	-0.75	2,200	25%	0.50

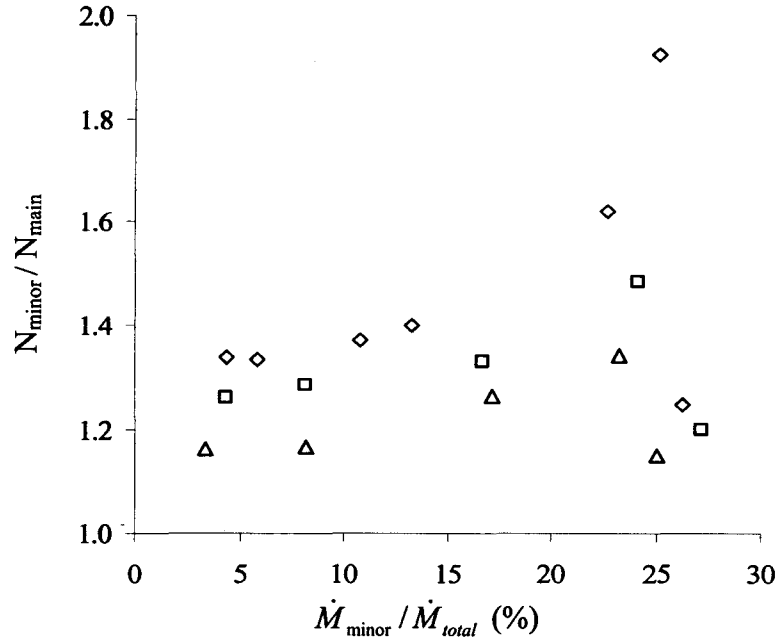

Figure 4.13 Change in PM concentration ratio with minor flow ratio at a lip position (S/D) of 1.5 and Reynolds numbers of △ 2,200, □ 14,000, ◇ 25,700

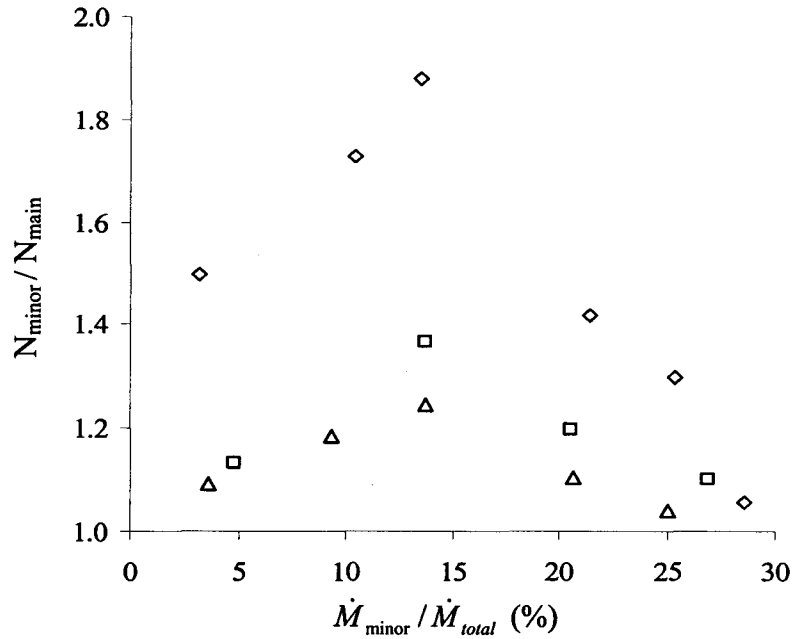

Figure 4.14 Change in PM concentration ratio with minor flow ratio at a lip position (S/D) of 0.75 and Reynolds numbers of △ 2,200, □ 14,000, ◇ 25,700

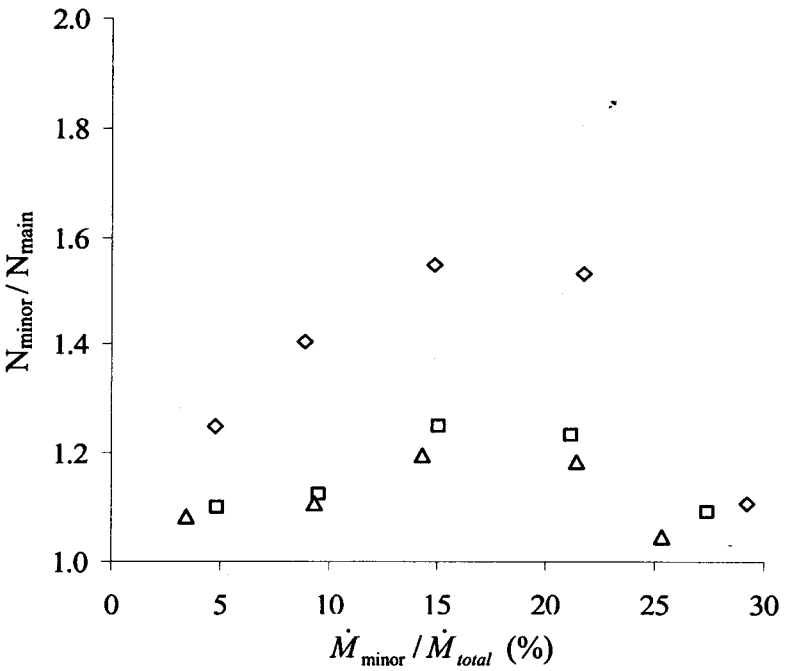

Figure 4.15 Change in PM concentration ratio with minor flow ratio at a lip position (S/D) of -0.75 and Reynolds numbers of △ 2,200, □ 14,000, ◇ 25,700

Table 4.5 The maximum concentration ratios in engine tests with the lip position, the inlet flow Reynolds number, and the minor flow ratio to the total

Lip position (S/D)	**Reynolds number (Re)**			**Optimum flow ratio** ($\dot{M}_{minor} / \dot{M}_{total}$)
	2,200	**14,000**	**25,700**	
-0.75	1.2	1.25	1.55	15%
0.75	1.24	1.36	1.88	13%
1.5	1.34	1.48	1.93	25%

of 0.75 and –0.75. For a smaller lip position value, when the flow ratio approaches the optimum concentration ratio, the change in the concentration ratio is not as sharp as that for the higher lip position value. The maximum concentration ratio values and the conditions at which this ratio occurs are listed in Table 4.5. The inlet flow Reynolds number also affects the maximum concentration ratio. The concentration ratio increased as the Reynolds number was increased. For the case with lip position of 1.5, the maximum concentration ratio increased 40% as the Reynolds number increased from 2,200 to 25,700. For the cases with lip position of 0.75 and –0.75, the concentration increased by 50% and 30% for the corresponding increase in Reynolds number. The lip position affects the concentration ratio but has less influence than the Reynolds number. The concentration ratio increases as the lip position is deeper in the concentration probe. For the case with a Reynolds number of 25,700, the maximum concentration ratio increased 21% as the lip position was changed from –0.75 to 0.75. When the lip position further changed from 0.75 to 1.5, the concentration ratio increased a further 5%. For the smaller Reynolds numbers, this effect was less significant.

In the concentration probe, the minor flow expands while the main flow streamline curvature occurs. The penetration depth of the main flow into the probe depends on the Reynolds number, the lip position, and the minor to total flow ratio. The separation of particles from the main flow to the minor flow is determined by the slopes of the main flow streamline curvature. For a fixed lip position in the virtual impactor, the curvature of the streamlines of the main flow are greater for larger inlet Reynolds numbers. The streamline curvatures are changed with the minor to the total flow ratio.

The slopes of the streamline curvature are the greatest at a certain optimum flow ratio. On the other hand, for a fixed inlet flow rate, the penetration depth of the main flow into the concentration probe is increased as the inlet tube is deeper in the probe. In this case, there is a shorter distance between the inlet tube lip and the concentrator wall and a higher flow ratio in the minor branch is required for the minor flow to expand to achieve the maximum curvature in the main flow streamlines.

Chapter 5 Conclusions

The virtual impactor type dust flow concentrator to concentrate the particulate matter in diesel engine exhaust into a low flow branch for subsequent removal using an electrostatic precipitator was evaluated in this study. The design of the virtual impactor uses a round inlet jet and a round concentration probe. These were integrated within a chamber using two circular end plates. The device has two outlets for the main flow and a singe outlet for the minor flow from the concentration probe. The inlet jet was designed so that its lip position relative to the concentration probe could be changed and a valve was installed in the minor branch to control the minor flow rate.

Experiments were performed to characterize the pressure loss and particulate matter concentration in the prototype virtual impactor type dust flow concentrator. Tests were performed in an air test rig and diesel engine exhaust test facility to determine the effect of the inlet flow Reynolds number, the lip position, and the fraction of the flow rate to the minor branch on the pressure drop across the device. The pressure loss was also numerically simulated for laminar flows in a simplified model of the flow concentrator. The pressure loss and particulate matter concentration effect was also investigated in a diesel exhaust rig for the different parameters listed above.

The pressure loss across the device increased with an increase in the inlet Reynolds number, a decrease in the minor to main flow ratio, or when the inlet tube was moved deeper into the concentrator probe. In all cases, changes in the inlet Reynolds

number had the most significant effects on the pressure loss. For example, in the air test, the increase in the pressure loss caused by the changes in lip positions reached at most 10% and the increase by decreasing the minor flow ratio was only 5%. On the other hand, the pressure loss coefficient increased by 80% as the Reynolds number increased from 33,500 to 46,500. In the engine test, the influences from the lip position and minor to main flow ratio were larger than those in the air test. For example, the increase due to changes in lip positions reached 20% and the increase due to change in minor to main flow ratio was up to 25%. This difference may be due to the gas-particle two-phase flow in the diesel engine exhaust flow.

It was found the pressure drop from the chamber to the outlet was 70% of the pressure drop across the device and the pressure loss from the inlet to the chamber is 30% of the total pressure loss for the Reynolds number ranging from 8,500 to 46,500. The pressure loss is mainly caused by the sharp changes in flow direction and flow cross sectional area from the chamber to the outlet. The pressure coefficients in engine tests are 30-40% less than the air tests at the corresponding Reynolds number. The pressure drop measurement results from the engine tests were within 10% to those from the simulations at the corresponding lower Reynolds number.

The particulate matter concentration ratio of the minor flow to that of the main flow was used to characterize the concentration effect for different conditions. The concentration ratio for each case had a maximum value that corresponded to an optimum minor flow ratio to the total and the concentration ratio distribution for the cases with the same lip position were similar. The flow ratio at which the concentration was a maximum

was mainly determined by the lip position. As the inlet tube was placed deeper into the concentration probe, there was a sharper change in the concentration distribution as the flow ratio approached the optimum ratio. The Reynolds number had a more significant effect on the value of the maximum concentration ratio compared to the lip position. For example, when the Reynolds number increased from 2,200 to 25,700, the concentration ratio increased up to 50% while the concentration ratio increased at most 25% as the lip position was changed from –0.75 to 1.5.

At its optimum operation, the particulate matter concentration ratio of the minor to main flow was 1.93 and the minor flow ratio to the total flow was about 30%. This is lower than what is required for successful operation of the flow concentrator for diesel engine exhaust particulate matter control. Suggestions for improvement are provided in chapter six.

Chapter 6 Recommendations

The virtual impactor in this study makes use of the particle inertial effect to concentrate the particulate matter into the minor flow. This effect becomes smaller for very fine particulate matter, and as a result a high inlet velocity is needed for this device. This can cause a high back pressure on the diesel engine. It is recommended to investigate the particle diffusion mechanism to concentrate the particulate matter in the diesel engine exhaust.

For the current device, the concentration effect for the particulate matter of the diesel engine exhaust in the flow concentrator was investigated based on mass concentration measurements in this work. These measurements cannot provide information on the particle size distribution, which is important to properly design of this device. Hence, it is recommended that measurements for the particle size distribution at the inlet and the outlets be performed. The particle number concentration can also be obtained from the particle size distribution.

The numerical simulations in this work were performed for a laminar single-phase flow in a simplified model. Additional simulations for turbulent inlet flows are needed since diesel engine exhaust flows are usually turbulent. It is recommended to investigate the particle behavior in the gas flow to take into account the interaction between the phases. The numerical model could be based on the particulate matter mass and size concentration distribution from the aforementioned tests.

To improve the particulate matter concentration or separation effect, it is recommended to use a smaller diameter tube for the higher inlet flow Reynolds number to yield a better concentration effect. However, the flow velocity in the inlet can reach very large values and the compressibility effects can become significant.

Future work is needed to optimize the concentrator geometry. It is recommended to use a concentration probe with different diameters in order to investigate its effect on the particulate matter concentration. For the future installation of the electrostatic precipitator, the chamber needs to be enlarged and the length of the outlet tubes need to be longer to leave space for the electrostatic precipitator. Another concern is about the gate valve in the minor branch. Since the flow through the gate valve is not axisymmetric, the flow streamline distribution in the concentration probe may be affected. Hence, it is recommended to use an orifice to replace the gate valve. Orifices with different sizes could be used to change the minor outlet to inlet diameter ratio.

The pressure loss needs to be minimized since it affects the performances of the concentrator and the diesel engine. In the current system, the friction loss is only a small fraction and the pressure loss is mainly due to the 'minor loss'. The 'minor loss' was caused by the sharp changes in the flow direction and the flow cross sectional area. The following two areas need to be considered. From the chamber to the main flow branch, the flow cross sectional area was sharply decreased. At the cross, the flow directions of the two main branches were opposite to each other and then sharply turned by 90 degrees to exit. It is recommended to use a reducer between the chamber plate and the main branch to gradually decrease the flow cross sectional area. Another recommendation is to

connect the two branches to a particular reducer by tube elbows. The angle of the elbow could be chosen to be much larger than 90 degree. The reducer has two inlets with the same size as the tube elbows. Each of the reducer inlets would be aligned with the elbow so the flow could pass through them without a change in flow direction.

Bibliography

Bagley, S.T., Baumgard, K.J., Gratz, L.G., Johnson, J.H., and Leddy, D.G., 1996. Characterization of fuel and aftertreatment device effects on diesel emissions. Research Report No.76, Health Effects Institute, Boston.

Barr, E.B., Hoover, M. D., Kanapilly, G. M., Yeh, H.C., Rothenberg, S.J., 1983. Aerosol Concentrator: Design, Construction, Calibration, and Use. Aerosol Science and Technology, vol. 2, pp.437-442.

Boyce, M.P. and Blick, E.F., 1969. Fluid Flow Phenomena in Dusty Air. ASME paper No. 69-WA/FE-24.

Chang, J.S. 2003. Next Generation Integrated Electrostatic Gas Cleaning System. Journal of Electrostatics, vol.57, pp. 273-291.

Chein, H., Lundgren D.A., 1993. A Virtual Impactor with Clean Air Core for the Generation of Aerosols with Narrow Size Distributions. Aerosol Science and Technology, vol.18, pp.376-388.

Chen, B.T., Yeh, H.C., 1987. An Improved Virtual Impactor: Design and Performance. Journal of Aerosol Science, vol.18, no 2, pp.203-214.

Chen, B. T., Yeh, H.C., Cheng, Y.S., 1985. A Novel Virtual Impactor: Calibration and Use. Journal of Aerosol Science, vol.16, no 4, pp.343-354.

Chen, B.T., Yeh, H.C., Cheng, Y.S., 1986. Performance of a Modified Virtual Impactor. Aerosol Science and Technology, vol.5, pp.369-376.

Cheng, Y.S. and Yeh, H.C., 1979. Particle Bounce in Cascade Impactors. Environmental Science and Technology, vol. 13, pp. 1392-1396.

Coleman, H.W., and Steele, W.G., 1999. Experimentation and Uncertainty Analysis for Engineers", John Wiley & Sons, New York.

Crowe, C.T., Troutt, T.R., Chung J.N., 1996. Numerical Models for Two-phase Turbulent Flows. Annular Review of Fluid Mechanics, vol.28, pp.11-43.

Crowe, C.T., 1981. On the Relative Importance of Particle-Particle Collisions in Gas-Particle Flows. Paper C78-81, Conference on Gas-Borne Particles, Institute of Mechanical Engineering, Oxford, England, pp. 135-137.

Crowe, C.T., 1982. Review: Numerical models for dilute gas-particle flows. Journal of Fluids Engineering, vol.104, pp.297-303.

Culick, F.E.C., 1964. Boltzmann Equation Applied to a Problem of Two-Phase Flow. Physics of Fluids, vol.7, pp.1898-1904.

Dockery, D.W., Pope III, A., Xu, X., Spengler, J.D., Ware, J.H., Fay, M.E., Ferris, Jr.B.G. and Speizer, F.E., 1993. An association between air pollution and mortality in six U.S. cities. Journal of medicine, vol.329, pp. 1753-1759.

Elghobashi, S.E., 1994. On predicting particle-laden turbulence flows. Applied Scientific Research, vol.52, pp.309-329.

Ergun, S., 1952. Fluid Flow Through Packed Columns. Chemical Engineering Progress, vol.48. pp.89-94.

Fan, Liang-Shih, Zhu, Chao, 1998. Principles of Gas-Solid Flows, Cambridge University Press, Cambridge, U.K.

Fang, C.P., Marple, V.A., Rubow, K.L., 1991. Influence of Cross-Flow on Particle Collection Characteristics of Multi-Nozzle Impactors. Journal of Aerosol Science, vol.22, pp.403-415.

Forney, L.J., Ravenhall, D.G., and Lee, S. S., 1982. Experimental and Theoretical Study of a Two-Dimensional Virtual Impactor. Environmental Science and Technology, vol.16, pp.492-497.

Friedlander, S.K., 1977. Smoke, Dust and Haze: Fundamentals of Aerosol Behavior, Wiley-Interscience, New York.

Fuchs, N.A., 1964. The Mechanics of Aerosols. Pergamon Press, New York.

Gotoh, K., Masuda, H., 2001. Development of Annular-Type Virtual Impactor. Powder Technology, vol.118, pp. 68-78.

Gidaspow, D., 1993. Hydrodynamic Modeling of Circulation and Bubbling Fluidized Beds. In Particulate Two-Phase Flow. Ed. M.C. Roco. Butterworth-Heinemann, Boston.

Hashimoto, S., Miyairi, Y., Hamanaka, T., Matsubara, R., Harada, T., and Miwa, S., 2002. SiC and Cordierite Diesel Particulate Filters Designed for Low Pressure Drop and Catalyzed, Uncatalyzed Systems. SAE paper No. 2002-01-0322.

Hesketh, H.E., 1977. Fine Paricles in Gaseous Media, Ann Arbor Science, Ann Arbor.

Hinds, W. C., 1982. Aerosol Technology: Properties, Behavior, and Measurement of Airborne Particles. John Wiley & Sons, New York.

Hounam, R. F., Sherwood, R.J. 1965. The Cascade Centripeter: A Device for Determining the Concentration and Size Distribution of Aerosols. American Industrial Hygiene Association Journal, vol. 26, pp. 122-131.

Jakab, G.J., et al., 1992. Use of physical chemistry and in vivo exposure to investigate the toxicity of formaldehyde to carbonaceous particles in the murine lung. Research Report No. 53, Health Effects Institute, Boston.

Jaenicke, R. and Blifford, I.H., 1974. The Influence of Aerosol Characteristics on the Calibration of Impactors. Journal of Aerosol Science, vol. 5, pp. 457-464.

Johnson, T.V., 2003. Diesel Emission Control in Review-the Last 12 Months. SAE paper No. 2003-01-0039.

Kane, R.S., 1989. Drag Reduction by Particle Addition. Viscous Drag Reduction in Boundary Layers, vol. 123. Progress in Astronautics and Aeronautics. Ed. Bushnell and Hefner. AIAA (American Institute of Aeronautics and Astronautics), Washington, D.C.

Kim, D.S., Kim, M.C., Lee, K.W., 2000. Design and Performance Evaluation of Multi-Nozzle Virtual Impactors for Concentrating Particles. Particle and Particle Systems Characterization, vol.17, pp. 244-250.

Kittelson, D.B., 1998. Engines and Nanoparticles, A Review. Journal of Aerosol Science, vol.29, pp. 575-588.

Konstandopoulos, A.G., et al., 2001. Inertial Contributions to the Pressure Drop of Diesel Particulate Filters, SAE paper No. 2001-01-0909.

Liebhaber, F.B., Lehtimäki, M. Willeke, K., 1991. Low-Cost Virtual Impactor for Large-Particle Amplification in Optical Particle Counters. Aerosol Science and Technology, vol.15, pp. 208-213.

Liu, Z. G., Skemp, M.D., Lincoln, J.C., 2003. Diesel Particulate Filters: Trends and Implications of Particle Size Distribution Measurement. SAE paper No. 2003-01-0046.

Loo, B. W., Cork, C. P., 1988. Development of High Efficiency Virtual Impactors. Aerosol Science and Technology, vol.9, pp.167-176.

Marcus, R.D., Leung, L.S., Klinzing, G.E., rizk, F., 1990. Pneumatic Conveying of Solids. Chapman & Hall, New York.

Marple, V. A., Chien, C.M., 1980. Virtual Impactors: A Theoretical Study. Environmental Science and Technology, vol.14, pp.976-985.

Marple, V.A., Liu, B.Y.H., Whitby, K.T., 1974. On the Flow Fields of Inertial Impactors. Journal of Fluids Engineering, vol. 96, pp.394-400.

Marple, V.A., Liu, B.Y.H., 1974. Characteristics of Laminar Jet Impactors. Environmental Science and Technology, vol.8, pp.648-654.

Marple, V.A., Willeke, K., 1976. Inertial Impactors: Theory, Design and Use. Fine Particles. Academic Press, New York

Masuda, H., Hochrainer, D., Stöber, W., 1979. An Improved Virtual Impactor for Particle Classification and Generation of Test Aerosol with Narrow Size Distribution. Journal of Aerosol Science, vol.10, pp. 275-287.

Mayer, A., Czerwinski, J., Scheidegger, P., 1996. Trapping Efficiency Depending on Particle Size. SAE paper No. 960472.

Miller, R.K., et al., 2002. Design, Development and Performance of a Composite Diesel Exhaust Emissions Control: Diesel Particulate Filters. SAE paper SP-1673.

Novick, V.J., Alvarez, J.L., 1987. Design of a Multistage Virtual Impactor. Aerosol Science and Technology, vol.6, pp.63-70.

Raber, L.R., 1997. EPA's air standards. Chemical and engineering news, April 14, 1997, vol. 75, pp. 10-18.

Rao, A.K. and Whitby, K.T., 1978. Non-Ideal Collection Characteristics of Inertial Impactors- I Single Stage Impactors and Solid Particles. Journal of Aerosol Science, vol.9, pp.77-86.

Rao, A.K. and Whitby, K.T., 1978. Non-Ideal Collection Characteristics of Inertial Impactors- II Cascade Impactors. Journal of Aerosol Science, vol.9, pp.87-100.

Rudinger, G., 1980. Fundamentals of Gas-Particle Flow. Elsevier, Amsterdam.

Scherrer, H.C., Kittleson, D.B., 1982. Light absorption cross sections of diesel particles. 1981 Transactions of SAE, SAE paper No.810181.

Schlichting, H., 1979. Boundary Layer Theory. 7th edition, McGraw-Hill, New York.

Sioutas, C., Koutrakis, P, Burton, R. M., 1994. Development of a Low Cutpoint Slit Virtual Impactor for Sampling Ambient Fine Particles. Journal of Aerosol Science, vol.25, pp.1321-1330.

Sioutas, C., Koutrakis, P., Burton, R.M., 1995. A Technique to Expose Animals to Concentrated Fine Ambient Aerosols. Environmental Health Perspectives, vol.103, pp.172-177.

Society of Automotive Engineers,1996. Volume 1: Materials, Fuels, Emissions, and Noise. 1996 SAE Handbook.

Soo, S.L., 1967. Fluid Dynamics of Multiphase Systems. Blaisdell, Waltham.

Soo, S.L., 1989. Particulates and Continuum: Multiphase Fluid Dynamics. Hemisphere, New York.

Soo, S.L., 1990. Multiphase Fluid Dynamics. Science Press, Beijing.

Svarovsky, L., 1981. Solid-Gas Separation. Elsevier, Amsterdam.

Szymanski, W.W., Liu, B.Y.H., 1989. An Airborne Particle Sampler for the Space Shuttle. Journal of Aerosol Science, vol.20, No. 8, pp.1569-1572.

Warheit, D.B., Seidel, W.C., Carakostas, M.C., Hartsky, M.A., 1990. Attenuation of perfluoropolymer fume pulmonary toxicity: Effect of fliters, combustion method, and aerosol age. Pulmonary Toxicity of Perfluoropolymer Fumes. Academic Press, pp.309-329.

Zhang, R., 2003. Master of Applied Science Thesis. Characterization of the EFR Cooling Device Used in Diesel Exhaust Gas Recirculation System, Department of Mechanical Engineering, McMaster University.

Zhou, L., 1993. Theory and Numerical Modeling of Turbulent Gas-Particle Flows and Combustion. Science press, Beijing.

Appendix: Modeling of Virtual Impactor

A.1 Introduction

The objective here was to evaluate the performance of an integrated particle removal system shown in Figure A.1. In this system, the incoming exhaust flow is separated into two flow branches in a dust flow concentrator and then the particulate matter from one branch is collected using an electrostatic precipitator. Ideally the branch passing to the electrostatic precipitator would have a low flow rate and high particulate matter concentration, while the other branch has most of the incoming flow but has a much lower particulate matter concentration. The concentrated particulate matter in the lower flow rate branch could then be collected in the electrostatic precipitator in the flow leg. The concentrator should have a simple geometry, a low pressure drop, and sharp particle separation cutoff performance.

It was proposed that the virtual impactor could work as the dust flow concentrator, but this has to be designed to determine its characteristics. A prototype of a round jet virtual impactor was chosen as the dust flow concentrator. A section of the impactor is shown in Figure A.2. It has a gradually contracting section at the bottom of the concentration probe. As the minor flow passes through the concentration probe to the outlet, the cross sectional area of flow is gradually decreased. The contracting section was also used to prevent the separated particles from depositing in the concentration probe.

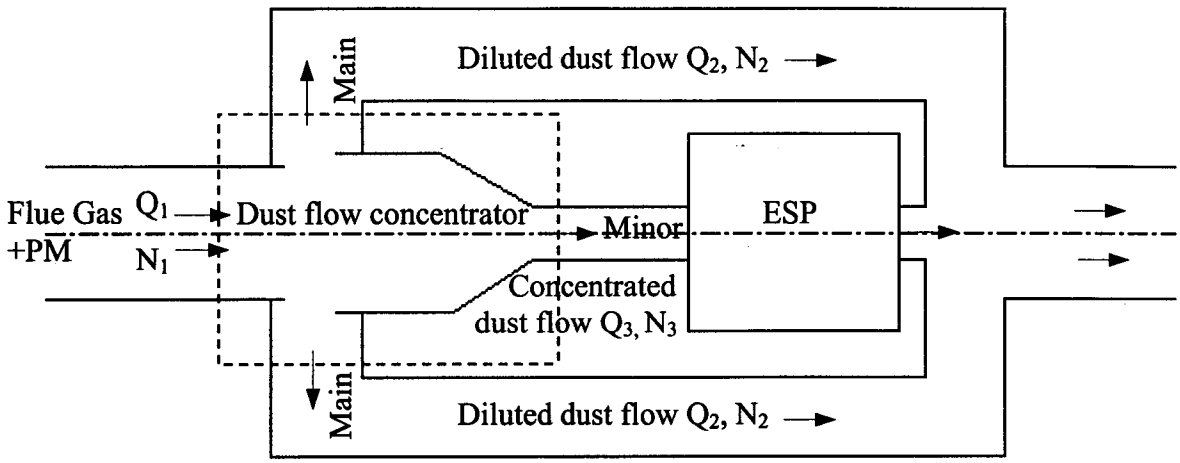

Figure A.1 Schematic of the proposed integrated particle removal system

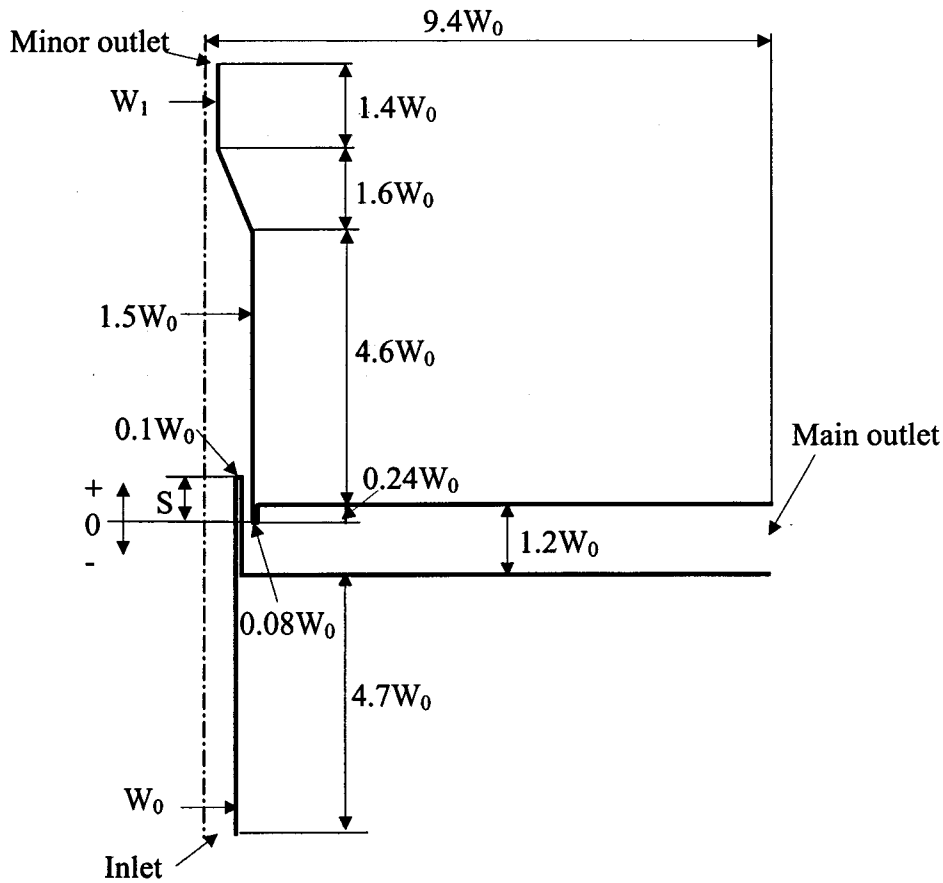

Figure A.2 Schematic of the virtual impactor prototype

The performance of this design was initially investigated using numerical simulation of the flow field and particle flow in the concentrator.

A.2 Numerical Simulations of the Flow Field

Numerical simulations were performed to investigate the flow field in the virtual impactor for the geometry shown in Figure A.2. The simulations were performed using the commercial software FEMLAB, which applies the finite element method to solve the incompressible Navier-Stokes equations. The simulations were performed for a two-dimensional section rather than an axisymmetric section.

The flow was assumed steady with constant fluid properties, i.e., air at 20 ℃ and standard atmospheric pressure and the simulation were performed for laminar flows. Due to the symmetric geometry, only the flow in half of the domain was considered as shown in Figure A.3. The boundary conditions for the fluid domain were set as follows. At the inlet, the flow was assumed fully developed laminar flow and the velocity profile was set as parabolic as shown in Figure A.4. The velocity gradient in x direction across the central line was set to zero and the no-slip boundary condition was used at the wall. At the minor branch outlet, the velocity gradient in y direction was zero while the velocity gradient in x direction was zero at the main branch outlet, i.e., it was assumed the flows at both exits were straight out. At both outlets, the pressure was assumed zero. Triangular elements were used in the mesh resolution. A typical overall mesh solution is shown in Figure A.5 that contains 6,049 nodes and 11,328 elements. The mesh resolution for the whole system was firstly set coarse and then refined in the areas that have relatively

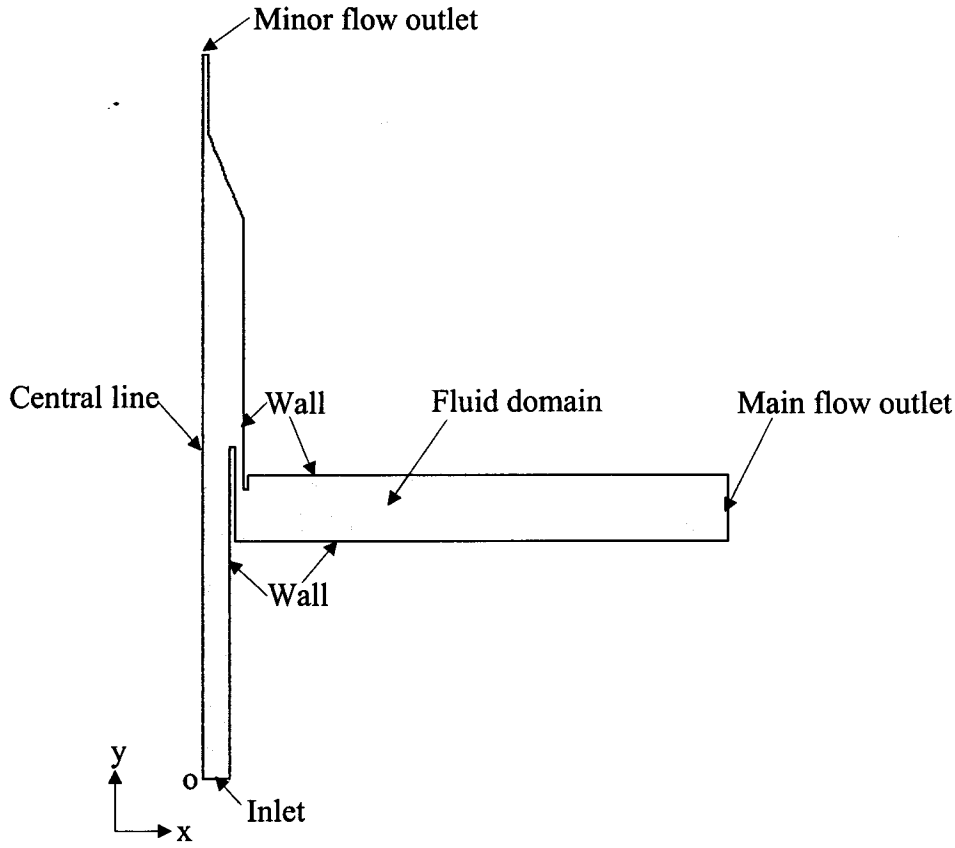

Figure A.3 Subdomain used for flow field simulation

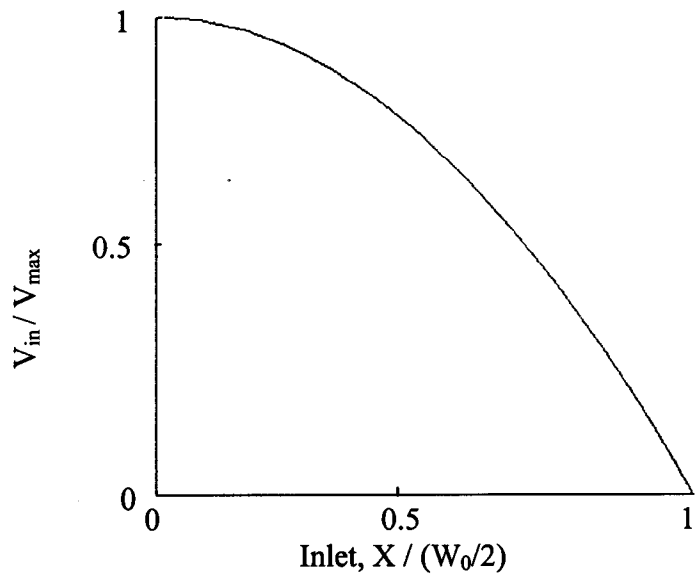

Figure A.4 The velocity profile at the inlet

complex geometry to better capture the large velocity gradient in these areas. There are two areas considered. One is the area containing the lips of the inlet jet tube and the concentration tube. The other is at the bottom of the concentration probe that has the contracting section. The refined meshes are shown in Figure A.6 and A.7 respectively.

The flow field was solved for a range of different minor outlet diameter to inlet diameter ratios, lip positions, and inlet flow rates to characterize how the flow distribution and pressure drop were affected by these parameters. The diameter ratio of the minor outlet to the inlet (W_1/W_0) ranged from 0.1 to 0.3. The relative lip position (S/W_0) was varied from –0.75 to 1.5. A typical flow streamline distribution for a Reynolds number of 500 is shown in Figure A.8. The minor diameter ratio to the inlet was 0.1 and the lip position was –0.75. In the concentration probe, the incoming flow is divided into the two branches, the minor flow branch and the main flow branch. The concentration probe is configured so that a major part of the flow is diverted to the main branch. The major flow experiences a sharp curvature in the streamlines in the concentration probe, which could allow for separation of the particulate matter from the gas flow. The main flow streamlines are parallel to the inlet tube as the main flow leaves the concentration probe and then turned by 180 degrees before entering the main flow branch. In the area where the main flow streamline curvature occurs, the minor flow streamlines begin to diverge and then converge at the probe contraction section. Recirculation zones were formed near the upper and lower corners of the main flow branch.

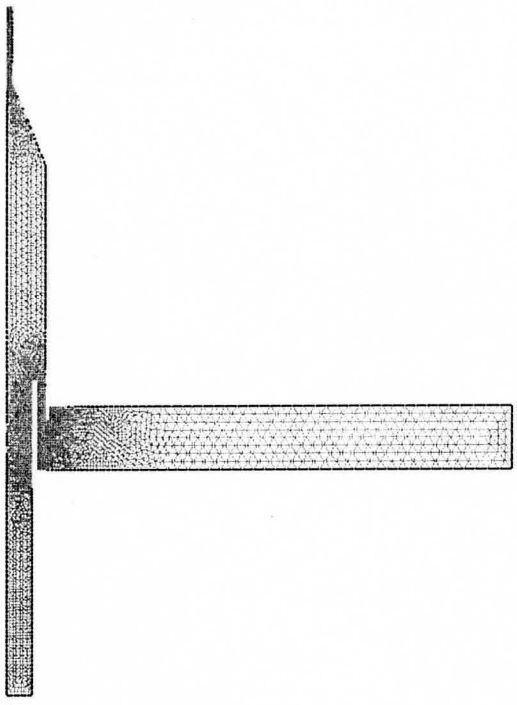

Figure A.5 Typical mesh resolution in the simulation

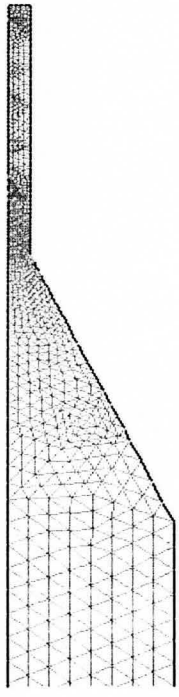

Figure A.6 Refined mesh for the contracting section

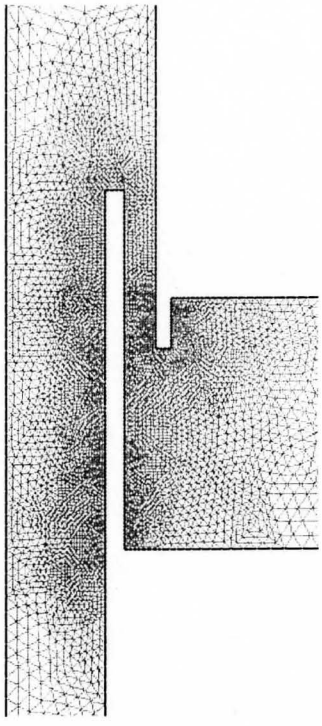

Figure A.7 Refined mesh for the flow separation area

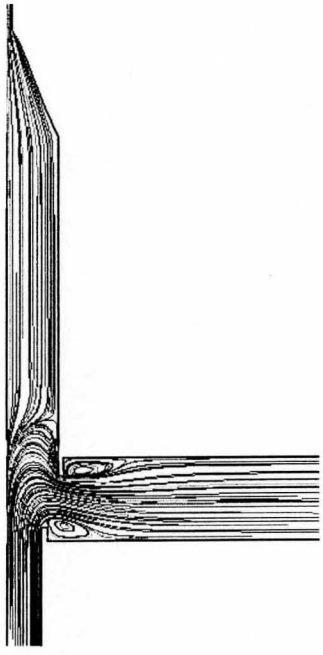

Figure A.8 Streamline distribution for inlet flow Reynolds number of 500 and lip position (S/W_0) of -0.75

A comparison was performed to evaluate the effects of the inlet Reynolds number and the lip position on the flow streamline distribution in the concentrator with minor outlet to inlet diameter ratio of 0.1. The effect of the inlet Reynolds number for the relative lip position of 1.5 are shown in Figure A.9, A.10, and A.11. Here, the streamline curvature and the penetration depth of the main flow in the concentration probe are of interest. As the inlet Reynolds number is increased, the penetration depth into the probe increases and the streamline curvature is increased. For example, for the flow with a Reynolds number of 500, the penetration depth is about 2 times the inlet tube diameter while for the flows with Reynolds number of 1,000 and 2,000, the penetration depth is about 5 and 7 times the inlet tube diameter, respectively. This sharper streamline curvature in the concentration probe results in higher accelerations which could improve the particle separation characteristics.

The lip position also influences the flow streamline distributions and recirculation zones. The effect of the lip position for an inlet flow Reynolds number of 2,000 are shown in Figure A.11, A.12, and A.13 for the lip positions of – 0.75, 0.75, and 1.5. When the lip position is –0.75, the lip of the inlet tube is outside of the concentration probe and only a portion of the total flow penetrates into the probe (Figure A.14). The curvature of the main flow streamlines are not as sharp as those with lip positions of 0.75 and 1.5. For example, the penetration depth for the lip position of –0.75 is 1.5 times of the inlet tube diameter while for the lip position of 0.75, this ratio is about 3. The recirculation zones are affected by the flow directions to the main flow branch. For the lip position of –0.75, a small recirculation zone was formed at the lower corner with a larger one at the upper

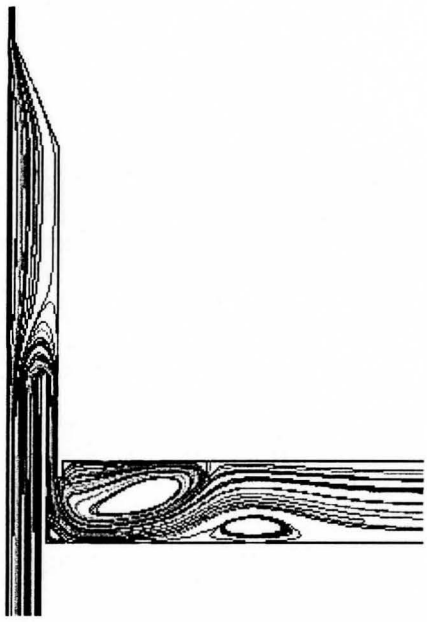

Figure A.9 Streamline distribution for inlet flow Reynolds number of 500 and lip position (S/W_0) of 1.5

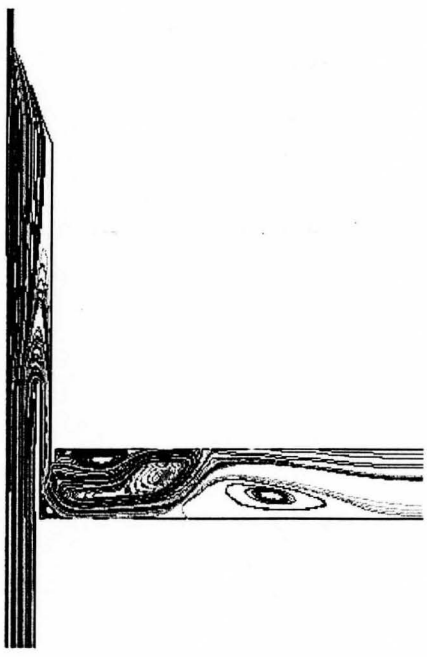

Figure A.10 Streamline distribution for inlet flow Reynolds number of 1,000 and lip position (S/W_0) of 1.5

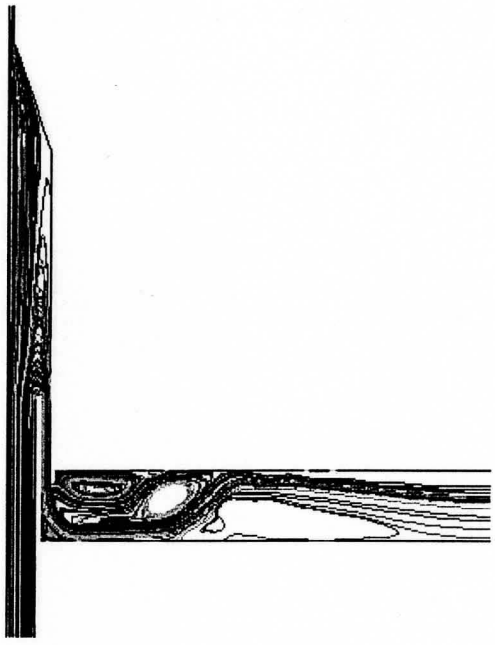

Figure A.11 Streamline distribution for inlet flow Reynolds number of 2,000 and lip position (S/W_0) of 1.5

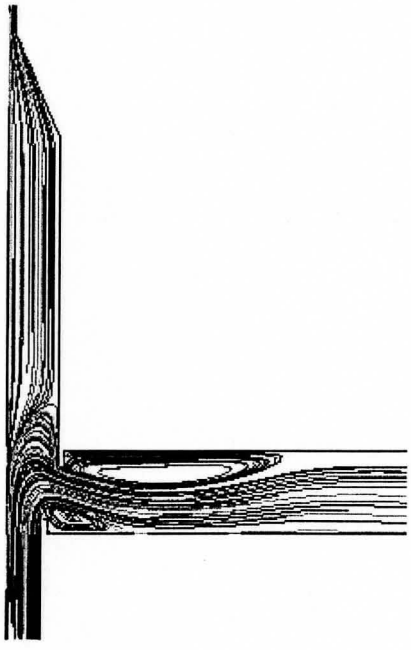

Figure A.12 Streamline distribution for inlet flow Reynolds number of 2,000 and lip position (S/W_0) of -0.75

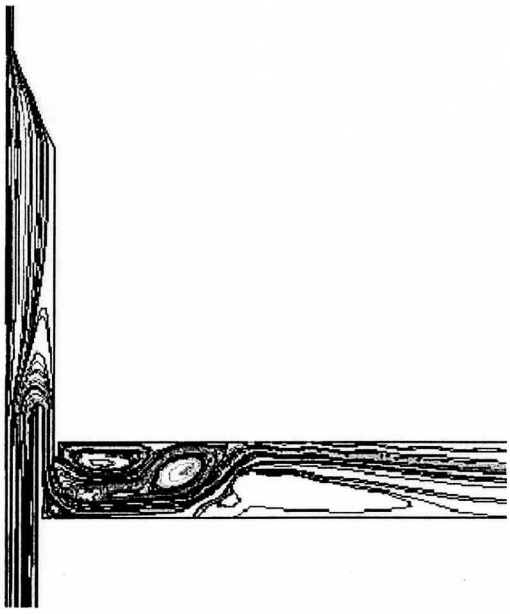

Figure A.13 Streamline distribution for inlet flow Reynolds number of 2,000 and lip position (S/W_0) of 0.75

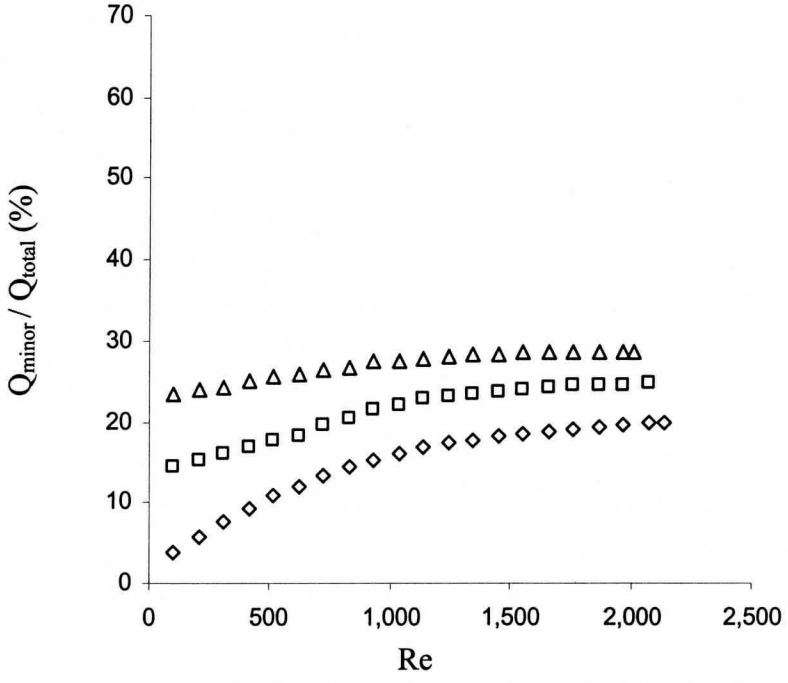

Figure A.14 Change in the minor flow ratio with the inlet Reynolds number for W_1/W_0=0.1 and lip positions (S/W_0) of ◇ -0.75, □ 0.75, Δ 1.5

corner. When the lip position was increased to 0.75 and 1.5, the extent of the smaller recirculation zone decreased while the larger zone divided into two zones with different extent. An additional recirculation zone develops further downstream near the lower branch plate as the lip position is increased.

A.3 Effect of Design on the Flow Rate Distribution and Pressure Drop

The inlet Reynolds number, the lip position, and the minor outlet to the inlet tube diameter ratio influence the flow distributions between the minor and the main flow. The change in the ratio of the minor flow passing through the end of the collector to the total flow with the inlet Reynolds number for diameter ratios of 0.1 and 0.2 are shown in Figure A.14 and Figure A.15. The relative lip distance (S/W_0) of –0.75, 0.75, and 1.5 are presented in these figures. The minor flow ratio increases with an increase in inlet Reynolds number. The relative increase, however, is different for the three different lip positions. For the (W_1/W_0) ratio of 0.1 and lip position of –0.75, the ratio increases sharply from 4% to 19% as the Reynolds number is increased from 100 to 1,500 and remains relatively constant beyond that. For the lip position of 0.75, the relative increase in minor to total flow ratio is smaller over the corresponding Reynolds number range, and reaches a maximum of approximately 25%. For the lip position of 1.5, the minor to total flow ratio increases only to a slightly higher value of 28%. Similar distributions are observed for a width ratio of 0.2, but in this case the steady minor to total flow ratio values are 46%, 50%, and 55% respectively, and are higher than the flow rates of interest here. In all cases, the flow ratio in the minor branch was relatively constant for Reynolds

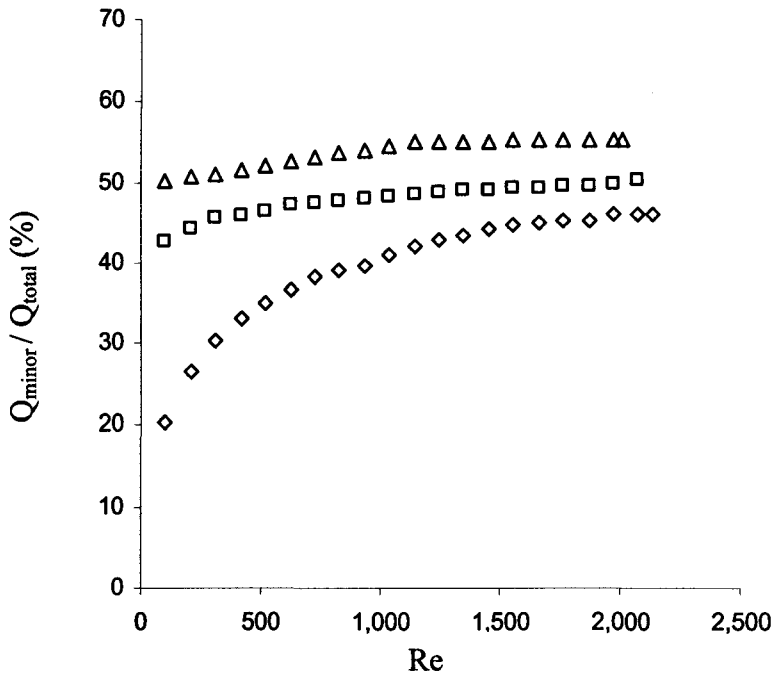

Figure A.15 Change in the minor flow ratio with the inlet Reynolds number for W_1/W_0=0.2 and lip positions (S/W_0) of ◇ -0.75, □ 0.75, Δ 1.5

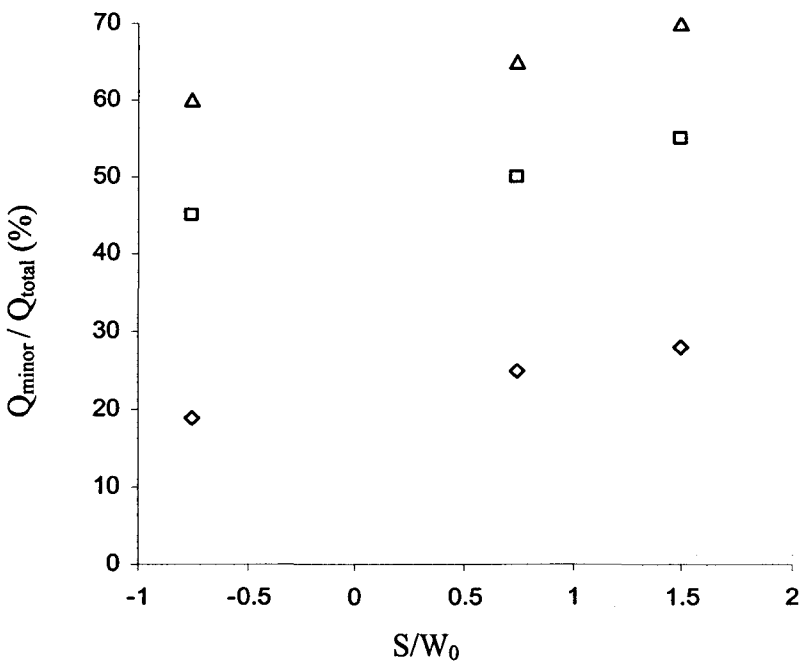

Figure A.16 Change in the minor flow ratio with the lip position for minor branch outlet diameter ratio to the inlet diameter (W_1/W_0) of ◇ 0.1, □ 0.2, Δ 0.3

numbers greater than about 1,500. The change of this relatively steady minor flow ratios with the three lip positions for minor outlet diameter ratio ranging from 0.1 to 0.3 is shown in Figure A.16. The lip positions affected the flow distribution but less than the minor branch outlet diameter. For example, for the case with the minor outlet diameter ratio of 0.1, the minor flow ratio to the total flow increased by 40% as the lip position was changed from –0.75 to 1.5. For the lip position of 1.5, the minor flow ratio to the total increased by 2.5 times as the minor outlet diameter ratio increased from 0.1 to 0.3. Inserting the inlet tube further into the concentration probe or increasing the minor outlet diameter would increase the streamline curvature required to turn the flow into the side branch and hence less flow would flow down the side branch.

An important parameter for the performance of a virtual impactor is the pressure distribution and the pressure drop across the device. A representative pressure distribution in the concentrator with the lip position of 0.75, minor diameter ratio of 0.1, and inlet Reynolds number of 2,000 is shown in Figure A.17. The pressure is a maximum in the concentration probe and drops sharply as the minor and the main flows leave the probe. The pressure variation along the central line of the concentrator for different lip positions and Reynolds numbers were evaluated. The normalized pressure variation along the central line for $W_1/W_0 = 0.1$ and the lip position of 1.5 at Reynolds number from 500 to 2,000 are shown in Figure A.18. The pressure decreases along the inlet tube and then sharply increases to a maximum value in the concentration probe. The pressure in the concentration probe is relatively steady before it decreases as the flow enters the contraction area. The normalized pressure increases with an increase in the Reynolds

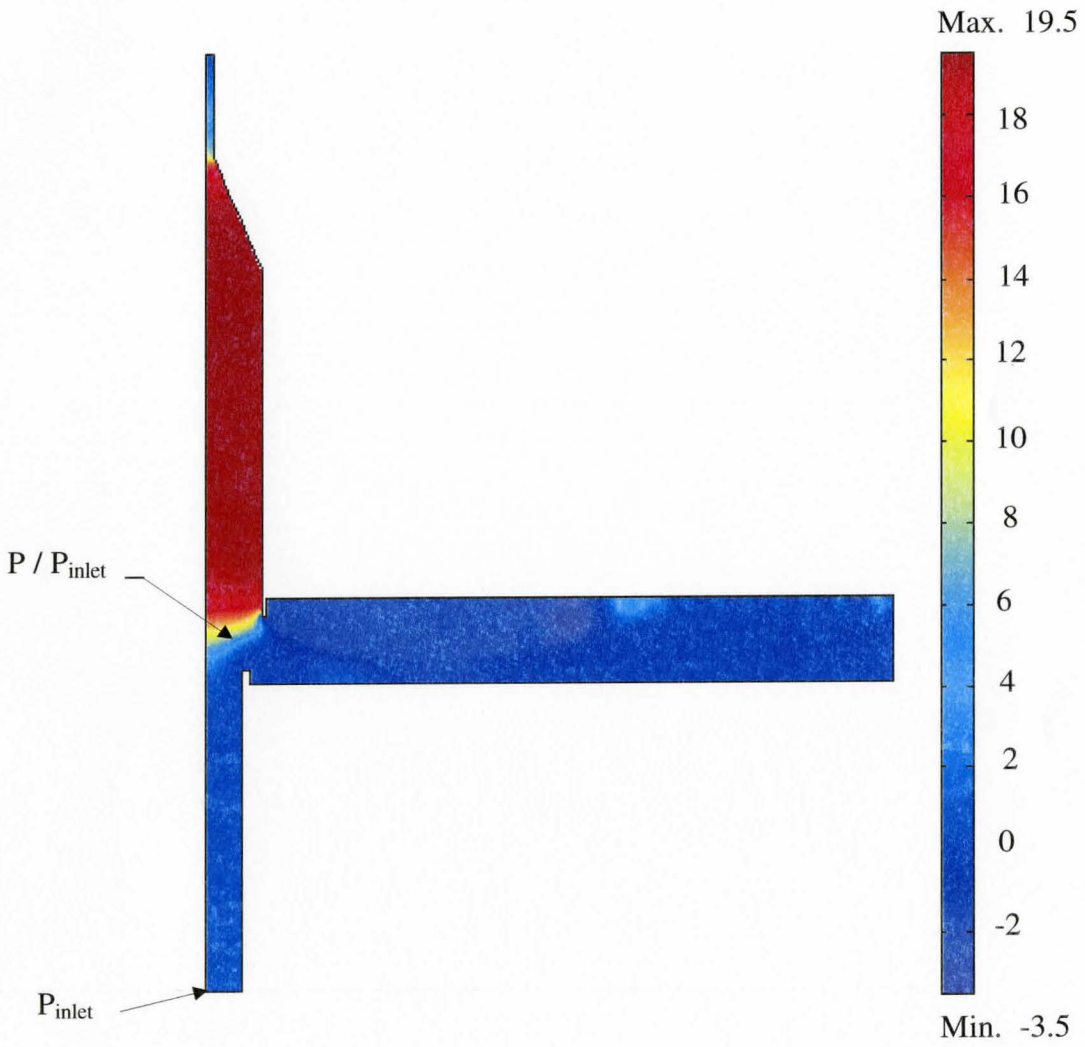

Figure A.17 The normalized pressure distribution in the virtual impactor for the lip position of -0.75, the minor outlet diameter ratio of 0.1, and inlet Reynolds number of 2,000

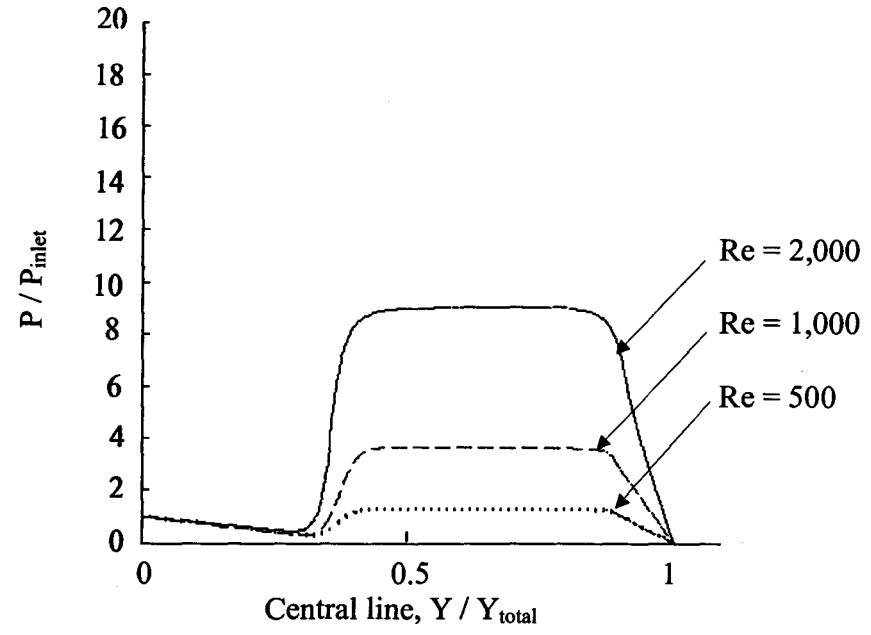

Figure A.18 Change in pressure ratio along the central line with lip position of 1.5 and Reynolds numbers of ·····500, -----1,000, and ——2,000

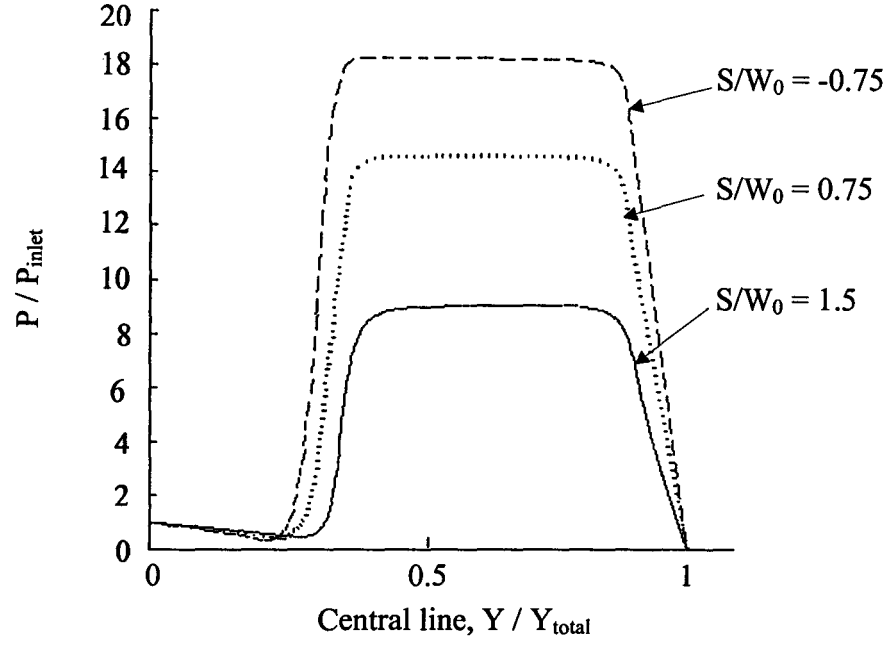

Figure A.19 Change in pressure ratio along the central line with Reynolds number of 2,000 and lip positions of -----0.75, ·····0.75, and ——1.5

number. For example, as the Reynolds number increased from 500 to 2,000, the pressure ratio in the probe increased by a factor of 7. This could be caused by the larger momentum flux of the flow at a higher Reynolds number. The previously presented flow rate distribution (Figure A.14 and Figure A.15) showed a larger flow fraction of the minor flow at a higher Reynolds number. The effect of lip positions on the pressure distribution at a Reynolds number of 2,000 and lip positions from –0.75 to 1.5 are shown in Figure A.19. The relative increase in the pressure decreases as the lip position is increased. For example, as the lip position increased from –0.75 to 1.5, the relative increase in the pressure in the concentration probe decreased from a factor of 18 to 9.

The pressure variation along the line from the inlet tube lip to the concentration probe was studied to evaluate its effects on the flow separation and streamline distribution in the minor and main flows. This line is parallel to the central line of the concentration probe. A representative result is shown in Figure A.20 for an inlet Reynolds number of 2,000, lip position of –0.75, and minor to inlet diameter ratio of 0.1. From the inlet tube lip to the concentration section, the pressure increases sharply over a short distance and then is relatively constant.

The change in the pressure drop coefficient across the virtual impactor with inlet flow Reynolds number for diameter ratio of 0.1 and 0.2 are shown in Figure A.21 and Figure A.22. Here, the pressure drop is the difference in the pressure from the inlet to the outlets. In all cases, the pressure drop coefficient decreased significantly as the inlet Reynolds number was increased to about 1,000. Beyond this, the pressure coefficient is relatively constant. The range of Reynolds number where the coefficient decreases

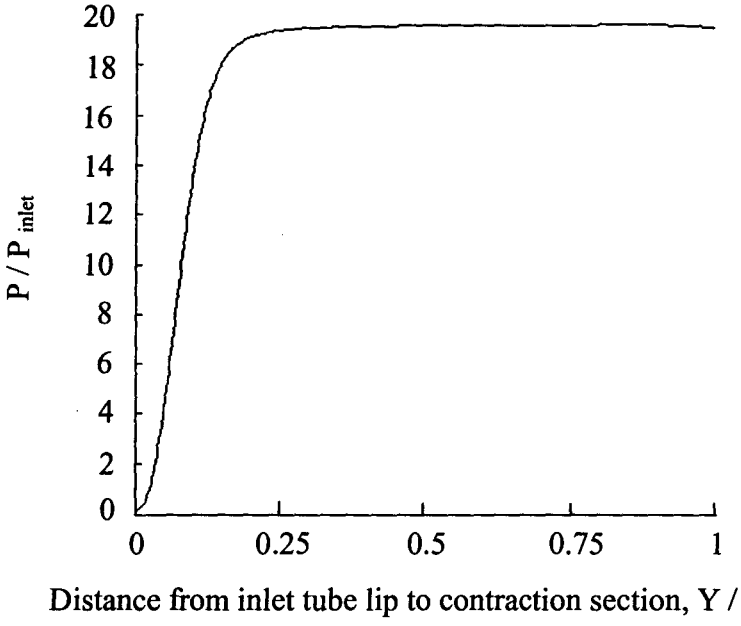

Figure A.20 Normalized pressure distribution along the line from inlet tube lip to contraction section with Reynolds number of 2,000, lip position of –0.75, W_1/W_0=0.1

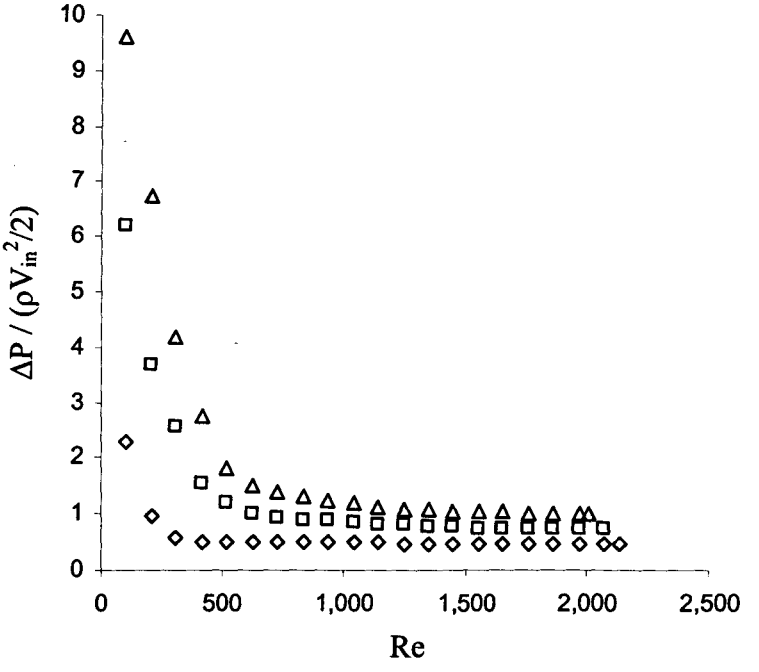

Figure A.21 Change in the pressure coefficient with the inlet Reynolds number for W_1/W_0=0.1 and lip positions (S/W_0) of ◇ -0.75, □ 0.75, Δ 1.5

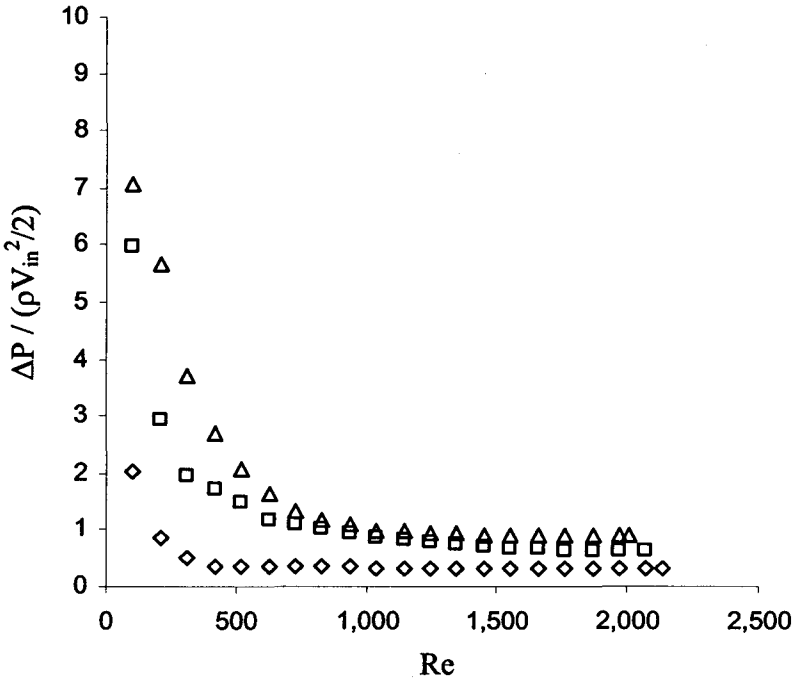

Figure A.22 Change in the pressure coefficient with the inlet Reynolds number for W_1/W_0=0.2 and lip positions (S/W_0) of ◇ -0.75, □ 0.75, Δ 1.5

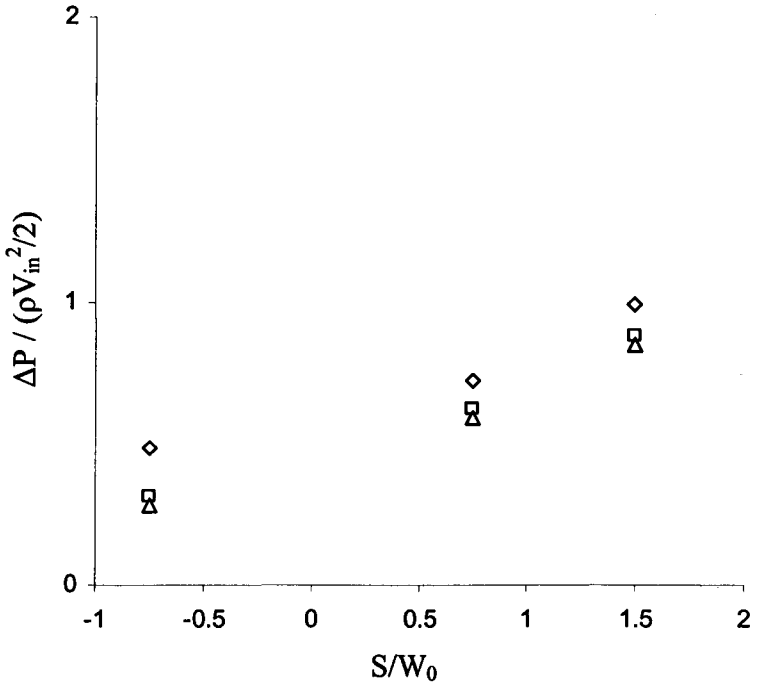

Figure A.23 Change in the pressure coefficient with the lip position for minor branch outlet diameter ratio to the inlet diameter (W_1/W_0) of ◇ 0.1, □ 0.2, Δ 0.3

changes with the lip position. For a lip position of 1.5, the coefficient decreases up to a Reynolds number of about 1,000, while for the lip position of -0.75 it decreases up to a Reynolds number of about 500. For a given inlet Reynolds number, the pressure coefficient increased as the lip was deeper into the concentration probe. The averaged pressure coefficient in the relatively constant region changes with the lip position and the minor branch outlet diameter ratio as shown in Figure A.23. The pressure coefficient decreased with an increase in the minor outlet diameter ratio. Both the lip position and the minor branch outlet diameter ratio affected the pressure loss coefficient, but the lip position has a more significant influence. For example, as the lip position was changed from -0.75 to 1.5, the pressure coefficient increased by 3 times while the increase due to the change in minor outlet ratio was within 40%.